The G protein-coupled receptor TBXA2R activates ERMs to promote motility, invasion, and metastasis of triple-negative breast cancer cells.

Kévin Leguay[1a], Omaima Naffati[1a], Yu Yan He[1a,1b], Mireille Hogue[1b], Chloé Tesnière[1c], Elena Melania Gombos[1c], Hellen Kuasne[3], Louis Gaboury[1d,2a], Christian Le Gouill[1b], Sylvain Meloche[1c,2b], Michel Bouvier[1b,2c#], Sébastien Carréno[1a,2a#]

[1]Institute for Research in Immunology and Cancer (IRIC), Université de Montréal, P.O. Box 6128, Station Centre-Ville, Montréal, QC H3C 3J7, Canada.
[1a] Cellular Mechanisms of Morphogenesis during Mitosis and Cell Motility lab
[1b] Molecular pharmacology lab
[1c] Signaling and Cell Growth lab
[1d] Histology and Molecular Pathology

[2] Université de Montréal, Montréal, Québec H3C 3J7, Canada
[2a] Department of Pathology and Cell Biology
[2b] Department of Pharmacology and Physiology
[2c] Department of Biochemistry and Molecular Medicine

[3]Department of Biochemistry, McGill University, Montreal, QC H3G 1Y6, Canada.

[#] These authors contributed equally to this work.

Corresponding authors:

M. Bouvier: michel.bouvier@umontreal.ca

S. Carréno: sebastien.carreno@umontreal.ca

ABSTRACT

Metastasis, the process by which cancer cells colonize distant organs, relies on the ability of these cells to migrate and invade the surrounding tissues. The ezrin, radixin, and moesin family (ERM) of proteins are critical regulators of cell morphology transformations required for cancer cell movement and invasion. Yet, how ERMs are activated during metastasis remains poorly understood. Here, we identified the thromboxane A2 receptor (TBXA2R), a G protein-coupled receptor, as a critical activator of ERMs that promotes motility, invasion, and metastasis of triple-negative breast cancer (TNBC) cells. We found that ERM activation downstream of TBXA2R signaling depends on the $G\alpha_{q/11}$ and $G\alpha_{12/13}$ subfamilies, the small GTPase RhoA, and its Ser/Thr kinase effector SLK. We also showed that TBXA2R signaling increases TNBC cell motility and invasion *in vitro* and metastasis *in vivo,* depending on ERMs. These findings unveil a novel mechanism by which a member of the largest class of receptors activates key metastatic determinants to promote TNBC metastasis, which could have important implications for developing novel therapeutic strategies.

INTRODUCTION

Ezrin, radixin, and moesin (ERMs) are a family of membrane-cytoskeleton linker proteins that regulate cell morphogenesis, migration, and invasion (Fehon et al., 2010). They integrate actomyosin forces and microtubule signaling at the cell cortex by crosslinking actin filaments (Algrain et al., 1993) and microtubules (Solinet et al., 2013) with the plasma membrane. Inactive ERMs cycle between the cytoplasm and the plasma membrane in a closed conformation, where their N-terminal FERM domain binds their C-terminal C-ERMAD domain (Leguay et al., 2021). Upon stimulation, ERMs open up and expose their FERM microtubule-binding domain (Solinet et al., 2013) and their C-ERMAD actin-binding site (Gary and Bretscher, 1995). The C-ERMAD also harbors a conserved regulatory threonine residue (T567, T564, and T558 in ezrin, radixin, and moesin, respectively) that is phosphorylated upon stimulation to maintain the active open conformation (Simons et al., 1998). ERMs were shown to control cell morphogenesis during mitosis (Carreno et al., 2008; De Jamblinne et al., 2020; Kunda et al., 2008; Leguay et al., 2022; Roubinet et al., 2011), cell migration (Arpin et al., 2011; Barik et al., 2022; Hoskin et al., 2015) and cell invasion (Estecha et al., 2009; Song et al., 2020). In a pathological context, high levels of ezrin, radixin, or moesin expression correlate with a high rate of metastasis and poor prognosis in several cancers (Clucas and Valderrama, 2014). For instance, increased expression of moesin correlates with the metastasis development of oral squamous cell carcinoma (Kobayashi et al., 2004), melanoma (Estecha et al., 2009), and breast carcinoma (Bartova et al., 2017). Radixin is overexpressed in prostate cancer (Bartholow et al., 2011). Ezrin is overexpressed and hyperactivated in several cancer cells, including metastatic rhabdomyosarcoma (Yu et al., 2004), osteosarcoma (Khanna et al., 2004), prostate cancer (Pang et al., 2004) and mammary carcinoma (Bruce et al., 2007). In mice, ERM inhibition prevents breast cancer or osteosarcoma cell metastasis (Elliott et al., 2005; Ghaffari et al., 2019). These examples and other observations led to the concept that ERMs play central roles in metastasis (Barik et al., 2022; Curto and McClatchey, 2004). ERMs are, therefore,

attractive targets for anti-cancer therapies. However, the mechanisms by which ERMs become activated during metastasis remain unknown.

Metastasis is responsible for most cancer deaths (Seyfried and Huysentruyt, 2013). This complex process is driven by the dysregulation of cell motility, which usually plays a crucial role in development and tissue repair. In cancer cells, aberrant signaling pathways activate cytoskeletal rearrangements to promote cell migration and enable invasion and dissemination to distant sites (Fife et al., 2014). In the last decade, evidence showed that cancer cells do not act alone but dialogue with surrounding cells and extracellular matrix components that promote tumor progression and metastasis (Clark and Vignjevic, 2015).

The thromboxane A2 receptor (TBXA2R) is a G protein-coupled receptor (GPCR) that mediates platelet activation and aggregation in response to thromboxane A2 (TXA2), a short half-life (~30 s) prostaglandin derivative (Jones et al., 1985). TXA2 also controls other functions, such as vasoconstriction, inflammation, and angiogenesis (Nakahata, 2008). In a pathological context, TXA2 promotes metastasis of several cancer, including colorectal (Guillem-Llobat et al., 2016), lung (Lucotti et al., 2019), prostate (Nie et al., 2004) and breast (Ekambaram et al., 2011) cancers. In addition, TBXA2R expression correlates with poor prognosis in aggressive breast tumors (Watkins et al., 2005), and targeting the TXA2 pathway has been proposed as a strategy against metastasis of these tumors (Li et al., 2017).

Breast cancer is a very heterogeneous disease that can be classified into subtypes based on the expression levels of different receptors. Among these subtypes, triple-negative breast cancer (TNBC) does not express estrogen, progesterone, and HER2 receptors. Both the high metastatic properties of TNBC cells and the lack of efficient, targeted therapy explain the high mortality rate of this cancer. While TNBC represents 10 to 20% of new breast cancer cases, it represents more than 30% of death associated with the disease (Bianchini et al., 2022). The physiology of TNBC metastatic cells is still poorly understood; thus, identifying the mechanisms that prompt these cells to disseminate could lead to developing more effective treatments for TNBC patients.

We recently demonstrated that RhoA, a small GTPase, activates ERMs at the onset of mitosis (Leguay et al., 2022). Interestingly, several GPCRs, including TBXA2R, are known to engage RhoA to achieve some of their functions (Yu and Brown, 2015). This prompted us to investigate the potential functional relationship between TBXA2R, RhoA, and ERMs. Here, we reveal a GPCR-RhoA-ERM signaling axis that promotes metastasis in TNBC. We discovered that TBXA2R engages the heterotrimeric G proteins $G\alpha_{q/11}$ and $G\alpha_{12/13}$ subfamilies, RhoA, and its kinase effectors SLK and LOK to activate ERMs in TNBC cells. Furthermore, we showed that activation of TBXA2R in these cells enhances cell migration and invasion *in vitro* and metastasis in a mouse xenograft model, depending on the activation of ERMs.

RESULTS

Activation of TBXA2R promotes ERM opening and activation.

In a first attempt to determine if TBXA2R activates ERM proteins, we took advantage of recently developed ERM conformational enhanced bystander BRET (ebBRET) biosensors that monitor the opening of individual ERMs at the plasma membrane (Leguay et al., 2021); the C-terminus of ezrin, radixin or moesin is fused to the bioluminescent energy donor *Renilla* luciferase (rLucII) while their N-terminus is anchored at the plasma membrane using a myristoylation signal and polybasic motif. The fluorescent energy acceptor *Renilla* GFP (rGFP) is also targeted to the plasma membrane by the prenylated CAAX motif of KRAS (rGFP-CAAX) (Fig S1A). In their closed, inactive conformation, ERMs are globular with a diameter of ~10 nm, while they open up to ~40 nm when activated (Liu et al., 2007). Since the transfer of energy between the BRET donor and acceptor is inversely proportional to their distance (Breton et al., 2010), the opening and activation of ERMs are measured by a decrease in ebBRET signals (Leguay et al., 2021). We first assessed the ability of TBXA2R to promote ERM opening and activation in HEK293 cells as these cells are well suited to study GPCR signaling using BRET assays (Breton et al., 2010; Gales et al., 2005; Kobayashi et al., 2019; Namkung et al., 2016; Namkung et al., 2018). Since TBXA2R is not expressed in these cells (Atwood et al., 2011), we co-transfected this GPCR with individual ERM biosensors and measured their ebBRET signal. This approach revealed that the three ERM proteins are opened downstream of TBXA2R. Activating this GPCR using U46619, a stable TBXA2R agonist (Coleman et al., 1981), decreased ebBRET signals associated with each ERM biosensor (Fig 1A and S1B-C). U46619 promoted ezrin, radixin, or moesin opening with a similar low nanomolar range EC50, in agreement with the affinity of this agonist for TBXA2R (Kattelman et al., 1986) (Fig 1B).

The phosphorylation of a conserved threonine residue stabilizes the ERM open, active form. We assessed this last step of ERM activation using an antibody that specifically recognizes p-ERM (Carreno et al., 2008), the phosphorylated forms of the three ERMs.

Confirming the results obtained with the ERM biosensors, U46619 promoted a substantial increase in phosphorylation of endogenous ERMs, almost similar to the increase triggered by calyculin A, a potent inhibitor of Ser/Thr phosphatases (Fig 1C-D). Furthermore, we found that ERM activation downstream of TBXA2R depends on the catalytic activity of a Ser/Thr kinase since staurosporine, a broad-spectrum kinase inhibitor prevents ERM phosphorylation upon U46619 treatment (Fig 1C-D). Consistent with these findings, staurosporine also prevented the U46619-induced ebBRET decrease in agreement with the role of phosphorylation in stabilizing the ERM open conformation (Fig 1A and S1B-C). We then characterized the timing of ERM activation downstream of TBXA2R and showed that U46619 triggers ERM phosphorylation very rapidly as the levels of p-ERM reach their maximum at 2 minutes, the earliest time-point tested. We also showed that this activation lasts at least 4 hours (Fig 1E-F).

Finally, immunofluorescence analysis of p-ERM revealed that TBXA2R activation increases ERM phosphorylation at the cell cortex, where ERMs crosslink the cytoskeleton with the plasma membrane (Fig 1G-H). Altogether, these experiments show that activation of TBXA2R promotes the opening and sustained activation of ERMs.

TBXA2R engages $G\alpha_{q/11}$, $G\alpha_{12/13}$, RhoA, and SLK kinases to activate ERMs.

Taking advantage of the versatility of HEK293 cells for transfection and loss-of-function experiments (Pulix et al., 2021), we aimed to identify the signaling pathway that TBXA2R engages in activating ERMs. Since TBXA2R activates ezrin, radixin, and moesin similarly (Fig 1B), we focused on the ezrin biosensor as a proxy to study ERM regulation. In accordance with U46619 activating ERMs through TBXA2R, U46619 did not affect ebBRET signals associated with the ezrin biosensor in cells that were not transfected with TBXA2R (Fig 1I). Further demonstrating the specificity of this newly discovered signaling axis, SQ-29548, a highly selective TBXA2R antagonist (Ogletree et al., 1985), prevented ezrin opening upon TBXA2R activation with U46619 (Fig 1J).

When activated, TBXA2R engages $G\alpha_{q/11}$ and $G\alpha_{12/13}$ sub-family members that relay the signal to different effectors (Avet et al., 2020; Nakahata, 2008). To characterize the role

of each of these two Gα sub-families in ERM activation, we used CRISPR-engineered HEK293 cells lacking the $G\alpha_{q/11}$ (Schrage et al., 2015) or $G\alpha_{12/13}$ (Devost et al., 2017) subunits ($\Delta G\alpha_{q/11}$ and $\Delta G\alpha_{12/13}$ cells, respectively). In $\Delta G\alpha_{q/11}$ cells, TBXA2R activation still promotes full ezrin opening, while deletion of $G\alpha_{12/13}$ subunits partially inhibited this opening (Fig 2A). We then tested whether $G\alpha_{q/11}$ and $G\alpha_{12/13}$ sub-families exert redundant functions in ERM activation downstream of TBXA2R. Treatment of $\Delta G\alpha_{12/13}$ cells with YM-254890, a selective inhibitor of $G\alpha_{q/11}$ subunits (Takasaki et al., 2004), completely inhibited ezrin opening upon TBXA2R activation (Fig 2A). This $G\alpha_{q/11}$ inhibitor did not affect ezrin opening in control parental cells downstream of TBXA2R activation, consistent with the results obtained with the deletion of $G\alpha_{q/11}$ subunits and confirming that either $G\alpha_{q/11}$ or $G\alpha_{12/13}$ subfamilies are sufficient to promote ERM opening.

Among the effectors of $G\alpha_{q/11}$ and $G\alpha_{12/13}$, RhoA was shown to promote phosphorylation and activation of ERMs (Bagci et al., 2020; Leguay et al., 2022; Shaw et al., 1998). We established that this small GTPase acts downstream of $G\alpha_{q/11}$ and $G\alpha_{12/13}$ subunits to activate ERMs. Indeed, treatment with the exoenzyme C3 transferase, a selective inhibitor of RhoA (Wilde and Aktories, 2001), prevented ezrin opening upon TBXA2R stimulation (Fig 2B).

We next aimed to identify which kinase(s) acts downstream of TBXA2R to activate ERMs. RhoA was shown to directly bind and activate two families of Ser/Thr kinases that can phosphorylate ERMs: the Rho-associated protein kinases ROCK1 and ROCK2 (Matsui et al., 1996) and the Ste20-like-kinase (SLK) and Lymphocyte-oriented-kinase (LOK) paralogs (Bagci et al., 2020; Leguay et al., 2022; Viswanatha et al., 2012). We previously showed that Y-27632, a specific ROCK inhibitor, inhibits ROCK kinases in HEK293 cells (Leguay et al., 2022). Here, we established that ROCK1 and ROCK2 do not activate ERMs downstream of TBXA2R since Y-27632 did not affect ezrin opening following U46619 treatment (Fig 2C). In contrast, transient depletion of SLK by RNAi reduced ezrin opening downstream of TBXA2R activation (Fig 2D). While the depletion of LOK led to a slight inhibition of ezrin opening, the co-depletion of both LOK and SLK paralogs completely prevented ezrin opening downstream of TBXA2R (Fig 2D). Consistent with kinases of the

SLK family being the sole kinases that relay the signal between TBXA2R and ERMs, inhibition of ROCK kinases with Y-27632 did not further reduce ezrin opening upon SLK, LOK or SLK/LOK transient depletion (Fig 2D). We then observed that LOK depletion has a minimal effect on ERM phosphorylation downstream of TBXA2R activation, as observed with the ezrin biosensor (Fig 2E-F). Conversely, SLK depletion almost completely abolished ERM phosphorylation, confirming the involvement of SLK as the primary kinase responsible for mediating the signal between TBXA2R and ERM activation in these cells. Furthermore, simultaneous depletion of SLK and LOK prevented any ERM phosphorylation, indicating that no other kinases are involved in this activation pathway.

Altogether, these results establish that TBXA2R activates RhoA through both $G\alpha_{q/11}$ and $G\alpha_{12/13}$, leading to ERM activation via kinases of the SLK family (Fig 2G).

TBXA2R activates ERMs in TNBC cells using the same signaling pathway identified in HEK293 cells.

Having shown that TBXA2R activates ERMs, we hypothesized that this signaling axis could promote motility, invasion, and metastasis of cancer cells. Given that TBXA2R and ERMs have previously been shown to regulate motility and invasion of TNBC cells individually (Orr et al., 2016; Qin et al., 2020), we investigated the potential involvement of the TBXA2R-ERM signaling axis in the metastasis of TNBC using model cell lines. We first established that TBXA2R activates ERMs in two different cellular models of metastatic TNBC, Hs578T and MDA-MB-231 cells (Dai et al., 2017; Hughes et al., 2008). At the difference of HEK293 cells, these cells express TBXA2R endogenously (Orr et al., 2016). Activation of endogenous TBXA2R by U46619 increased ERM phosphorylation at the cortex in both TNBC cell lines (Fig 3A-D and S2A-D).

We confirmed the pharmacological selectivity of action of the TBXA2R agonist in both TNBC cell lines by showing that the TBXA2R antagonist SQ29548 blocks ERM phosphorylation downstream of TBXA2R activation (Fig 3A-B and S2A-B). As we observed in HEK293 cells, U46619 activates ERMs in Hs578T cells at nanomolar potency

(Fig 1B and 3E-F). We also established that $G\alpha_{q/11}$ and $G\alpha_{12/13}$ subunits, RhoA and SLK, act downstream of TBXA2R to activate ERMs in Hs578T cells. We tested the role of the two Gα sub-families using YM-254860 to inhibit $G\alpha_{q/11}$ subunits and by overexpressing p115-RGS-CAAX, a previously characterized dominant-negative construct that inhibits $G\alpha_{12/13}$ activity (Lukasheva et al., 2020). In this construct, the RGS domain of p115-RhoGEF that regulates $G\alpha_{12/13}$ signaling (p115-RGS) is targeted at the plasma membrane using a CAAX motif. As observed in HEK293 cells, inhibition of $G\alpha_{q/11}$ alone did not reduce activation of ERMs downstream of TBXA2R. In contrast, inhibition of $G\alpha_{12/13}$ partially prevented ERM activation as measured by western blot analysis of p-ERM (Fig 3G-H). Yet, co-inhibition of both Gα sub-families further reduced ERM activation (Fig 3G-H). In addition, inhibition of RhoA using exoenzyme C3 transferase but not inhibition of ROCK kinases using Y-27632 prevented phosphorylation of ERMs upon TBXA2R activation (Fig 3I-J). Finally, transient depletion of SLK using two independent siRNAs almost totally abrogated ERM phosphorylation downstream of TBXA2R (Fig 3K-L). Consistent with this result, we demonstrated that TBXA2R activates SLK kinase activity, as measured by a ~2.5-fold increase in phosphorylation of the ezrin C-terminus *in vitro* using immunoprecipitated SLK from Hs578T cells treated with U46619 (Fig 3M).

TBXA2R activates SLK and moesin to potentiate TNBC cell 2D motility and 3D invasion.

We then investigated the role of the TBXA2R-ERM signaling axis in TNBC cell motility and invasion *in vitro*. To this end, we individually deleted individual ERMs by CRISPR-Cas9 editing of Hs578T cells. While the deletion of ezrin or radixin did not affect the increased phosphorylation of endogenous ERMs upon TBXA2R activation, the deletion of moesin almost totally abolished ERM phosphorylation (Fig 4A-B). We confirmed this finding by knocking-down ezrin, radixin, or moesin in Hs578T cells by stably expressing shRNA targeting each ERM (Fig S3A). Since TBXA2R activates ezrin, radixin, or moesin similarly (Fig 1B), these results suggest that moesin is the most abundant ERM expressed in Hs578T cells. This hypothesis was confirmed by analyzing the gene expression of Hs578T cells, based on single-cell RNA sequencing data available in the

Single Cell Expression Atlas (Papatheodorou et al., 2020), which revealed that moesin mRNA is expressed at the highest level among the three ERMs in Hs578T cells (Fig S3B). We thus decided to further study the role of the TBXA2R-ERM signaling axis by using the Δmoesin Hs578T cells.

To measure the motility of Hs578T cells, we used a modified version of the wound-healing scratch assay (Oris™) (Fig 4C). Cells migrating into the free area were followed for 6 hours, a timescale during which ERMs remained activated by U46619 in Hs578T cells (Fig S3C-D). We found that upon TBXA2R activation, Hs578T cells migrated ~1.5 faster than not stimulated cells (Fig 4F-G). The deletion of moesin by CRISPR-Cas9 using two independent single guide RNA significantly slowed down cell migration compared to controls (Fig 4D-G and S3E-F), confirming the importance of ERMs for cell migration (Arpin et al., 2011). Our results showed that activation of ERMs via TBXA2R increases the migration potential of Hs578T cells, as demonstrated by the lack of increased motility in two independent Δmoesin Hs578T cell lines following activation of this GPCR (Fig 4F-G). This finding underscores the importance of moesin in mediating the effect of TBXA2R on Hs578T cell migration. Confirming this finding, the depletion of moesin by shRNA promoted the same cell motility defects downstream of TBXA2R activation (Fig S3G). Finally, transient depletion of SLK using two independent siRNA revealed that this kinase, which activates ERMs downstream of TBXA2R, is essential for potentiating the migration of cells promoted by this GPCR (Fig 4H).

To investigate the role of the TBXA2R-ERM signaling axis during cell invasion, Hs578T cells were embedded and seeded in an extracellular collagen matrix (ECM) using the wound-healing scratch assay (Oris™) (Fig 4I). Cells invading the free zone filed with ECM with serum as a chemoattractant, were then tracked. This revealed that activation of TBXA2R by U46619 increases the speed of Hs578T cell invasion into the ECM by ~1.5 fold (Fig 4J). As observed for 2D cell migration, moesin and SLK were necessary for TBXA2R to potentiate cell invasion into the ECM. Moesin knock-out or SLK knock-down prevented TBXA2R from potentiating invasion of TNBC cells (Fig 4J-K). Our findings

establish that activation of ERMs via SLK downstream of TBXA2R is a key mechanism by which this GPCR promotes cell migration and invasion in TNBC cells.

Moesin is necessary for TBXA2R to potentiate metastasis of TNBC.

Upon analyzing RNA sequencing data from TNBC samples obtained from the Cancer Genome Atlas of Invasive Breast Carcinoma (Cancer Genome Atlas, 2012), we observed that TNBC exhibited higher levels of TBXA2R mRNA expression compared to normal breast tissues (Fig 5A). Further analysis revealed that only a subset of TNBC patients exhibited higher expression levels of this GPCR compared to normal breast tissues (Fig 5B). Interestingly, we also observed that overexpression of both TBXA2R and moesin in the same TNBC tumor was associated with poor overall survival (Fig 5C). These findings suggest that the TBXA2R-ERM signaling axis may play a critical role in TNBC progression and may be a potential therapeutic target for this subtype of breast cancer.

To investigate whether ERMs are activated downstream of TBXA2R signaling in tumor cells, we examined the levels of phosphorylated ERMs in TNBC biopsies in a tissue microarray (TMA). Our analysis revealed a positive correlation between TBXA2R expression and p-ERM levels in 55 TNBC samples (Fig 5D-E, $r=0.50$, $p=0.0001$). Three distinct subsets of TNBC were identified based on the levels of ERM phosphorylation and TBXA2R expression. The first subset had low levels of both p-ERMs and TBXA2R, suggesting that ERM activation plays a minor role if any in the cancer biology of this group. In contrast, the other two subsets exhibited high levels of p-ERMs, with one subset co-expressing high levels of TBXA2R. Notably, we did not observe any TNBC sample with high TBXA2R expression and low levels of p-ERMs, providing further evidence that TBXA2R signaling promotes ERM activation in TNBC.

We then tested if TBXA2R signaling could potentiate TNBC metastasis through ERM activation *in vivo*. To this end, we used a tail vein metastasis assay in immunodeficient NSG mice treated or not with the TBXA2R agonist U46619 (Fig 5F). Twenty-four days after injection, the size of liver tumor nodules and the liver tumor load was compared between control Hs578T cells and the two Δmoesin cell lines previously described.

Administration of U46619 was well tolerated and we did not observe any change in the body weight or weight of the liver (Fig S4A-B). In mice injected with control Hs578T cells, histopathological analysis of serial liver sections revealed that U46619 increases the size of metastatic nodules along with the liver tumor burden without affecting the number of nodules per animal (Fig 5G-I and S4C). Activation of TBXA2R resulted in a significant increase in the percentage of mice exhibiting liver surface with more than 10% of tumor cell invasion, from 25% (2 out of 8 mice) to 60% (6 out of 10 mice), confirming the crucial role of this GPCR in metastasis (Fig 5I). Our findings also showed that mice injected with Δmoesin Hs578T cells presented fewer metastatic nodules in their livers compared to those injected with control cells (Fig S4C). In contrast to mice injected with control Hs578T cells, treatment with U46619 did not increase the average size of liver metastatic nodules nor the liver tumor load when Δmoesin Hs578T cells were injected (fig 5G-I). As a result, none of the mice injected with Δmoesin cells showed a metastatic burden of more than 10% of their liver surface (Fig 5I). Notably, the differences in nodule size or tumor load observed across the different groups were not due to an effect of U46619 on the growth of metastatic cells. We found that U46619 did not affect the proliferation of control or Δmoesin cells *in vitro* (Fig S4D) nor *in vivo* since the Ki-67 proliferative index of these cells was similar in the liver of every animal (Fig 5J-K).

DISCUSSION

Our study sheds light on the involvement of a GPCR-ERM signaling pathway in cancer cell metastasis. We have found that the G protein-coupled receptor TBXA2R activates proteins of the ERM family, promoting cancer cell motility and invasion *in vitro* and metastasis in a xenograft model. This signaling pathway depends on the $G\alpha_{q/11}$ and $G\alpha_{12/13}$ subfamilies, which converge on RhoA, activating kinases of the SLK family that promote ERM activation.

While previous studies have identified ROCK, SLK, and LOK kinases as direct effectors of RhoA (Bagci et al., 2020; Matsui et al., 1996), our findings revealed that downstream of TBXA2R and RhoA, ERMs are primarily activated by SLK, and to a lesser extent, LOK. SLK depletion almost completely abolished ERM phosphorylation following TBXA2R-mediated RhoA activation, indicating that SLK is the primary kinase in this pathway responsible for ERM activation. However, our experiments also showed that LOK could partially compensate for SLK depletion in HEK293 cells, as demonstrated with the ezrin ebBRET biosensor. This suggests that LOK may have a role in maintaining ERM activation downstream of TBXA2R under specific conditions.

Recently, we reported that RhoA activates SLK to drive metaphase cell rounding by activating ERMs at the mitotic cortex (Leguay et al., 2022). We found that two different Rho-GEF, GEF-H1 and Ect2 activate RhoA at mitotic entry. Here we showed that ERM activation depends on RhoA downstream of $G\alpha_{q/11}$ and $G\alpha_{12/13}$ subfamilies. While $G\alpha_{q/11}$ inhibition alone did not prevent ERM activation downstream of TBXA2R in HEK293 and TNBC cells, genetic depletion of $G\alpha_{12/13}$ partially prevented this activation. It is only when both Gα subfamilies are inhibited that TBXA2R signaling fails to activate ERMs. This indicates that whereas $G\alpha_{12/13}$ is the main Gα subfamily engaged by TBXA2R to activate ERMs, $G\alpha_{q/11}$ can partially compensate for the loss of $G\alpha_{12/13}$. Several Rho-GEF such as p63RhoGEF, p115RhoGEF, pDZ-RhoGEF, GEF-H1, and LARG (Lutz et al., 2007; Meiri et al., 2014; Nakahata, 2008; Sah et al., 2000; van Unen et al., 2016; Wikstrom et

al., 2008) were shown to be activated by $G\alpha_{12/13}$ or $G\alpha_{q/11}$ and represent possible links between these G proteins and the RhoA activation. .

While GPCRs and ERMs are intensively studied, only a few studies have reported a link between these two families of proteins. For instance, activation of the muscarinic M1 receptor (M1R) or the β2-adrenergic receptor (β2AR) by their respective agonists was shown to promote ezrin activation through the G protein-coupled receptor kinase 2 (Cant and Pitcher, 2005). Thrombin that activates PAR1, PAR3, and PAR4 was also reported to allow the recruitment of radixin at the plasma membrane of endothelial cells upon direct binding of this ERM to $G\alpha_{13}$ (Vaiskunaite et al., 2000). Lysophosphatidic acid (LPA), which activates $LPARs_{1-6}$ also promotes the activation of moesin in platelets (Nakamura et al., 1995; Retzer and Essler, 2000; Shcherbina et al., 1999). More recently, LPA activation of $LPAR_1$ and $LPAR_2$ was found to stimulate the phosphorylation of ERMs in the ovarian cancer cell line OVCAR-3 (Park et al., 2018). Interestingly, expression of $ezrin^{T567A}$, a non-phosphorylatable mutant of the regulatory threonine that acts as a dominant negative form of ERMs, reduced the migration of OVCAR-3 cells toward LPA, used as a chemoattractant.

Our study establishes the signaling cascade that connects the G protein-coupled receptor TBXA2R to ERM activation, which ultimately promotes TNBC cell migration, invasion and metastasis. While it is currently unclear whether alternative mechanisms proposed for other GPCRs, such as the involvement of GRK2 (Cant and Pitcher, 2005) or direct binding of ERM to $G\alpha_{13}$ (Vaiskunaite et al., 2000) contribute to ERM activation downstream of TBXA2R, our findings demonstrated that kinases of the SLK family are the only kinases needed for ERM activation by TBXA2R. Therefore, any potential contribution from other mechanisms would need to occur upstream of these two kinases. It is also unclear whether $G\alpha_{q/11}$ and/or $G\alpha_{12/13}$ are the only G proteins that mediate the activation of ERM downstream of the other GPCRs found to activate ERMs. However, it is noteworthy that M1R, β2AR, Thrombin-activated PARs, as well as $LPAR_{1/2}$, were found to activate either $G\alpha_{q/11}$ or $G\alpha_{12/13}$ or both (Avet et al., 2022).

The molecular basis underlying metastasis is still incompletely understood, and the mechanisms that prompt cancer cells to disseminate to secondary organs can be very diverse. These mechanisms depend on genetic alterations of cancer cells, but they also rely on the interaction of cancer cells with the stroma (Welch and Hurst, 2019). Thromboxane A2 (TXA2), the natural ligand of TBXA2R, was found to promote metastasis in colorectal (Guillem-Llobat et al., 2016), lung (Lucotti et al., 2019), prostate (Nie et al., 2004) and breast (Ekambaram et al., 2011) cancers, opening the possibility that TBXA2R can be targeted to prevent metastasis. Supporting this hypothesis, Ifetroban (CPI211), a potent and selective antagonist of TBXA2R, was recently shown to reduce the metastasis burden of several cancer cell lines, including TNBC cells, in xenograft mouse models (Werfel et al., 2020). Ifetroban is currently being evaluated in a clinical trial (NCT03694249) as a potential treatment for high-risk solid tumors that are prone to metastatic recurrence. The rationale of this trial is that Ifetroban inhibits TBXA2R on platelets, which reduces their aggregation on cancer cells, ultimately preventing platelet-assisted metastasis (Lucotti et al., 2019; Werfel et al., 2020).

Our study identifies a distinct mechanism by which TBXA2R could be targeted to block metastasis; activation of TBXA2R on TNBC cells can increase their motility, invasion, and metastatic potential by activating ERMs. Overexpression of essential components of this pathway could upregulate this TBXA2R-ERM signaling axis. Supporting this notion, we found that simultaneous overexpression of TBXA2R and moesin mRNAs is associated with poor overall survival in a subset of TNBC patients. We also found that TBXA2R expression correlates with phosphorylation and activation of ERMs. Since TBXA2R signaling is a potent activator of ERMs, activation of this GPCR by its natural ligand, TXA2, could also promote metastasis by activating ERMs. TXA2 might be secreted by the tumor cell itself in an autocrine signaling loop, by a subpopulation of other tumor cells, or by cells of the stromal microenvironment, in paracrine signaling loop. Supporting a paracrine activation by cells of the microenvironment, platelets that naturally secrete TXA2 were shown to interact with tumor cells to promote metastasis (Gay and Felding-

Habermann, 2011). Additionally, platelets were also shown to induce the expression of TXA2 by colon cancer cells to stimulate metastatic dissemination (Dovizio et al., 2015), suggesting that paracrine activation by microenvironmental cells could be a significant factor. The precise role of the TBXA2R-ERM signaling axis in these contexts remains to be investigated. Finally, other potential sources of TXA2 are infiltrating macrophages and endothelial cells of tumor blood vessels that naturally secrete TXA2 and could therefore prompt cancer cells expressing TBXA2R to metastasize.

Identifying therapeutic targets for metastasis is challenging due to its complexity, and so far, no effective anti-metastatic drugs have been approved for clinical use (Anderson et al., 2019). However, the discovery that TBXA2R activates ERMs through $G\alpha_{12/13}$ and $G\alpha_{q/11}$ suggests that other GPCRs that engage one of these two Gα subfamilies could also promote metastasis by activating ERMs. Given that several GPCR antagonists are already approved drugs or have advanced to clinical for other indications, repurposing them for anti-metastatic treatment could be accelerated. Moreover, our characterization of the TBXA2R-ERM signaling pathway could identify novel therapeutic targets to prevent metastasis. While ERMs are already promising therapeutic targets (Clucas and Valderrama, 2014; Ghaffari et al., 2019; Hoskin et al., 2019; Ren and Khanna, 2014), their activating kinases, SLK and LOK, also show promise as potential targets to prevent metastasis.

ACKNOWLEDGMENT

This work has been supported by a project Grant from the CIHR (175193) to S.C. and M.B., a Foundation Grant from the CIHR (148431) to M.B. and a Cancer Research Society grant (25388) to S.M. K.L held a doctoral scholarship from Institute for Research in Immunology and Cancer (IRIC) and from Montreal University's Molecular Biology Program as well as a Études Supérieures et Postdoctorales (ESP) studentship from Montreal University. O.N. holds a master and doctoral scholarship from the Mission Universitaire de Tunisie en Amérique du Nord, from Montreal University's Molecular Biology Program as well as from IRIC. C.T. held a doctoral studentship from the Fonds

de recherche Santé Québec. M.B. held the Canada Research Chair in Signal Transduction and Molecular Pharmacology. The authors declare no competing financial interests.

AUTHOR CONTRIBUTIONS

Management of the project: K.L., C.L.G, M.B, SC. Conceptualization: K.L., C.L.G, S.M, M.B, SC. Investigation: K.L., O.N, Y.Y.H, M.H, C.T, E.M.G, H.K. Formal Analysis: K.L., O.N, H.K, C.L.G, S.M, M.B, S.C. Resources: L.G. Writing – Original Draft: K.L, M.B, S.C. Writing – Review and Editing: K.L, C.L.G, S.M, M.B, S.C. Visualization: K.L, H.K, S.C. Funding acquisition: S.M, M.B, S.C.

MATERIAL AND METHODS

Reagents and inhibitors

Coelenterazine 400a (Deep Blue C) was purchased from NanoLight Technology (#340). U46619 and SQ-29548 were purchased from Cayman Chemical (#16450 and #19025, respectively). Calyculin A and Y-27632 ROCK inhibitors were purchased from Sigma (#C5552 and #688000, respectively). Staurosporine was purchased from ApexBio (#A8192). Rho inhibitor I (C3 transferase) was purchased from Cytoskeleton (#CT04). YM-254890 was purchased from FUJIFILM Wako Pure Chemical Corporation (#257-00631).

DNA constructs

The cDNA for TBXA2R was previously described (Parent, JBC 1999). (MyrPB-)ezrin-, radixin-, moesin-rLucII, and rGFP-CAAX constructs were previously described (Leguay, JCS 2021). MISSION shRNA constructs were obtained in pLKO.1-puro vectors from Sigma: EZR (TRCN0000062459), RDX (TRCN0000062434), MSN (TRCN0000062412). FlexiTube siRNA were obtained from Qiagen: SLK#1 (SI00107723), SLK#2 (SI04438350), LOK (SI02224054).

Cell culture and transfection

HEK293T human kidney cells, Hs578T, and MDA-MB-231 TNBC cells were maintained in Dulbecco's modified Eagle's medium (DMEM; 4.5 g/L D-Glucose, L-Glutamine, 110 mg/L sodium pyruvate; Thermofisher #11995073) supplemented with 10% fetal bovine serum (FBS; Life Invitrogen #12483020) and 1% penicillin-streptomycin antibiotics (ThermoFisher #15070063) at 37°C with 5% CO_2. HEK293T cells knock-out for $G_{q/11}$ or $G_{12/13}$ were obtained from Asuka Inoue (Tohoku University, Japan). Hs578T cell clones knock-out for ezrin, radixin, or moesin were obtained by CRISPR-Cas9, followed by clonal dilution after selection with 2 µg/ml puromycin (EMD Millipore #540222) for 48h. The following sequence guide were inserted in plentiCRISPR-v2 (addgene #52961)

digested with BsmBI (New England Biolabs #R0739): EZR (CTGAGCGGCTGATCCCTCAA), RDX (GTTTCACTTACCGCTGGGGT), MSN#1 (GAGACAAGTTGCTCCCGCAG) and MSN#2 (AAGCTTACCTGAGCATGCCA).

For ebBRET experiments, HEK293T cells were transfected using linear polyethyleneimine (PEI, Alfa Aesar #43896) as previously described (Leguay, JCS 2021). Loss of function experiments were performed by transfecting siRNA using lipofectamine RNAiMAX (Thermofisher #13778075) as prescribed by the manufacturer or by infecting cells with lentiviral particles in DMEM supplemented with 10% FBS and 5 µg/ml polybrene (Sigma #H9268) for 48h followed by a 48h-treatment with 2 µg/ml puromycin.

ebBRET measurement

rbBRET measurements were performed as previously described (Leguay, JCS 2021). Briefly, 48h after transfection, HEK293T cells were washed with Hank's balanced salt solution (HBSS, ThermoFisher #14065056) and incubated for 5 min with 2.5 µM coelenterazine 400a diluted in HBSS. ebBRET signals were monitored using a Tecan Infinite 200 PRO multifunctional microplate reader (Tecan) equipped with BLUE1 (370-480 nm; donor) and GREEN1 (520-570 nm; acceptor) filters. ebBRET signals were calculated as a ratio by dividing the acceptor emission value by the donor emission value.

Immunoblotting

Following indicated treatment, cells were washed with ice-cold phosphate-buffered saline (PBS) and lysed in TLB buffer (40 mM HEPES, 1 mM EDTA, 120 mM NaCl, 10 mM NaPPi, 10% glycerol, 1% Triton X-100, 0.1% SDS) supplemented with both phosphatase and protease inhibitors (phosphatase inhibitor cocktail (PIC, Sigma #P2850), 1 mM sodium orthovanadate (Na_3VO_4, Sigma #S6508), 5 mM β-glycerophosphate (Sigma #G6251), 1 mM phenylmethylsulfonyl fluoride (PMSF, Sigma #P7626) and anti-protease cocktail (Sigma #4693132001)). Samples were then denatured in sample buffer (200 mM Tris-HCl 1M pH6.8, 8% SDS, 0.4% bromophenol blue, 40% glycerol, and 412 mM β-

mercaptoethanol) and resolved by SDS-PAGE followed by transfer to nitrocellulose membranes (pore 0.2µm, VWR #27376-991). Membranes were blocked in TBS-Tween (25 mM Tris-HCl pH 8, 125 mM NaCl, 0.1% Tween 20) supplemented with 2% BSA for one hour before overnight incubation with primary antibodies at 4°C. Primary antibodies were: rabbit anti-p-ERM (1:5000, Roubinet 2011), rabbit-anti ERM (1:1000, Cell Signaling #3142), rabbit anti-Ezrin (1:1000, Cell Signaling #3145), rabbit anti-Radixin (1:1000, Cell Signaling #2636), rabbit anti-Moesin (1:1000, Cell Signaling #3150), mouse anti-Actin (1:5000, Sigma #MAB1501), rabbit anti-SLK (1:1000, Cerdalane #A300-499A) and rabbit anti-LOK (1:5000, Abcam #ab70484). Washed membranes were then incubated for 1h at room temperature with secondary antibodies: goat anti-rabbit-IgG HRP (1:10000, Santa Cruz biotechnology #sc-2004) and goat anti-mouse-IgG HRP (1:10000, Santa Cruz Biotechnology #sc-516102). Protein detection was finally performed using Amersham ECL Western Blotting detection reagent (GE Healthcare #CA95038-564L).

In vitro kinase assay

In vitro kinase assays were performed as previously described (Leguay, JCB 2022). Briefly, HEK293T cells treated with U46619, or its vehicle were lysed in TLB buffer supplemented with phosphatase and protease inhibitors. Endogenous SLK was then immunoprecipitated from cell lysate using rabbit anti-SLK antibody (Bethyl #A300-499A) incubated for 1h at 4ºC, followed by incubation with protein A-sepharose beads (GE Healthcare #GE17-0780-01) for 2h at 4ºC. Beads were then extensively washed and resuspended in kinase reaction buffer (KRB; 50 mM Tris-HCl pH 7.5, 100 mM NaCl, 6 mM $MgCl_2$, and 1 mM $MnCl_2$) supplemented with both phosphatase and protease inhibitors, 2 mM DTT, 50 µM ATP and purified recombinant GST-Ezrin$^{479-585}$ from BL21 bacteria. Kinase assay was finally performed for 30 min at 30ºC, and proteins were denatured with sample buffer.

Immunofluorescence

The day before the experiment, cells were plated on glass coverslips (Marienfeld #0115200) and incubated at 37°C with 5% CO_2 overnight. Cells were then washed with PBS and fixed with 10% trichloroacetic acid (Sigma #T0699) for 10 min at room temperature, followed by extensive washes with TBS (20mM Tris-HCl pH 7.5, 154 mM NaCl, 2mM EGTA, 2mM $MgCl_2$). Cells were then permeabilized with 0.02% saponin (Amresco #0163) diluted in TBS supplemented with 2% BSA (Bioshop #ALB001.250) for 1h. Cells were then incubated overnight with rabbit anti-p-ERM primary antibody (1:5000, Roubinet, 2011) followed by goat anti-rabbit Alexa Fluor 488-conjugated secondary antibody (1:200, Invitrogen #A11070) for 1h. Glass coverslips were finally mounted in Vectashield medium with DAPI (Vector Laboratories #H-1200), and images were acquired using an LM700 confocal microscope (Zeiss) with 63x objective.

Cell migration and invasion assay

Migration experiments were performed using the Oris™ Cell Migration assay (Platypus technologies) as the manufacturer prescribed. Briefly, Hs578T cells were plated in DMEM supplemented with 10% FBS in a 96-well plate with stoppers creating a central cell-free detection zone. The next day, stoppers were removed, and media was replaced with DMEM supplemented with 10% FBS and 10 nM U46619 or vehicle. Cells could then migrate into the free area.

Invasion experiments were performed using the Oris™ Cell Invasion assay (Platypus technologies) as prescribed by the manufacturer. Briefly, Hs578T were plated embedded in DMEM supplemented with 2 mg/ml collagen type I (rat tail) (Fisher scientific #CB354249) in a 96-well plate with stoppers creating a central cell-free detection zone. After collagen polymerization, stoppers were removed, and DMEM supplemented with 10% FBS and 2 mg/ml collagen type I was added to the central cell-free detection zone. After collagen polymerization, DMEM supplemented with 10 nM U46619, or vehicle was added on top of collagen. Cells could then invade into the free area.

Migration and invasion of cells into the free zone were recorded by contrast video microscopy using LSM700 confocal microscope (Zeiss) with 20x objective for 6 or 24 hours, respectively. Individual cells were manually tracked using the Manual Tracking plugin on ImageJ software (NIH). Cell velocity was determined as a ratio by dividing the total distance v over time. Representations of cell migration were obtained using Chemotaxis and Migration Tool 2.0 (Ibidi).

Immunohistochemistry

Tissue microarray was obtained as previously described (Yousef et al., 2014). Samples were obtained from the *Centre Hospitalier de l'Université de Montréal* (CHUM) after approval by the research ethical committee (Comité d'éthique de la recherche du CHUM CENTRE DE RECHERCHE, Approval No. SL 05.019).

Livers excised from mice were fixed in 10% formalin, embedded in paraffin, and sliced into 4-µm-thin sections. Tissue sections were mounted on glass slides and stained with hematoxylin and eosin (H&E) using conventional protocols. Immunohistochemical assays were performed on the Bond RX Stainer (Leica Biosystems, Buffalo Grove, IL, USA) according to the manufacturer's instructions. Briefly, slides were deparaffinized, and antigen recovery was conducted by heat-induced epitope retrieval with standard CC1 and CC2 solutions (Ventana Medical Systems, Tucson, AZ). Sections were then incubated with primary antibody for 30 min. Primary antibodies used are the following: p-ERM (1:600, Roubinet 2011), TBXA2R (1:100, Cayman chemicals #10004452) and Ki-67 (1:150, Biocare Medical #CRM325B). Bound primary antibodies were detected using peroxidase polymer (HRP-DAB) for 15 min. The stained slides were next subjected to digital slide scanning that converts glass slides into high-resolution digital data by high-speed scanning using the NanoZoomer Digital Pathology (NDP) 2.0-HT digital slide scanner (Hamamatsu, Japan). Signal intensities for p-ERM and TBXA2R were quantified at the plasma membrane using Image J software (NIH). Quantification of Ki-67-positive cells was performed using Visiomorph software (Visiopharm).

In vivo metastasis assay

Hs578T cells (5.0×10^4) were resuspended in 100 µl PBS and injected into the tail vein of NSG mice. Two days before cell injection and during the whole experiment, NSG mice were treated with U46619 (50 µg/kg) or vehicle (DMSO) administered through drinking water containing 0.1% aspartame (TCI chemicals #A0997), given ad libitum and changed every second day. The mice were then euthanized 24 days after cell injection in a CO_2 chamber. At the time of euthanasia, the liver was photographed and weighed, and the number of tumors was manually assessed under a stereo microscope. The left lobe was then processed for histological analysis.

Cell proliferation assay

Cell proliferation was measured using MTT. Briefly, Hs578T cell lines were seeded into 96-well plates in quadruplicate and cultured for the times indicated in the figure legend. The medium was then replaced with fresh medium supplemented with 1.1 mM MTT (Cayman chemical #21795), and cells were incubated at 37ºC for 4h. Dissolution of formazan was then performed by incubating cells with 67% DMSO at 37ºC for 10 min. Cell proliferation was assessed by reading the absorbance at 540 nm using a Tecan Infinite 200 PRO multifunctional microplate reader (Tecan).

Data analysis

All quantifications were performed using Image J software (NIH) and analyzed using GraphPad PRISM software (GraphPad Software, La Jolla, CA, USA). Microscopy images were prepared using Image J software (NIH) and Photoshop (Adobe).

FIGURE LEGENDS

FIGURE 1: Stimulating TBXA2R activates ERMs in HEK293T cells.

(**A**) ebBRET signals measured in HEK293T cells expressing MyrPB-ezrin-rLucII, co-transfected with TBXA2R (HEK293T-TBXA2R) and treated with vehicle, 100 nM U46619 for 5 min and/or 100 nM staurosporine for 30 min.

(**B**) ebBRET signals measured in HEK293T-TBXA2R cells expressing MyrPB-E,R,M-rLucII and treated with increasing concentrations of U46619 for 5 min.

(**C-D**) Immunoblots of HEK293T-TBXA2R cells treated with vehicle, 100 nM staurosporine for 30 min, 100 nM U46619 for 5 min, and/or 100 nM calyculin A for 10 min (**C**). p-ERM over ezrin signals were quantified and normalized to the vehicle (DMSO, **D**).

(**E-F**) Immunoblots of HEK293T-TBXA2R cells treated with 100 nM U46619 for the indicated times (**E**). p-ERM over ERM signals were quantified and normalized to the vehicle (t=0, **F**).

(**G-H**) Immunofluorescence of HEK293T-TBXA2R cells treated with vehicle or 100 nM U46619 for 5 min (**G**). p-ERM staining at the cell periphery was quantified and normalized to cells treated with vehicle (**H**).

(**I**) ebBRET signals measured in HEK293T cells expressing MyrPB-ezrin-rLucII and co-transfected with or without TBXA2R and treated with vehicle or 100 nM U46619 for 5 min.

(**J**) ebBRET signals were measured in HEK293T-TBXA2R cells expressing MyrPB-ezrin-rLucII biosensor and treated with vehicle, 100 nM U46619 for 5 min and/or 1 µM SQ-29548 for 30 min.

ebBRET signals (**A-B, I-J**) represent the mean +/- s.d. of three independent experiments. Immunoblots (**C, E**) and immunofluorescences (**G**) are representative of three independent experiments. P-ERM quantifications (**C**, **D**) represent the mean +/- s.d. of three independent experiments. Dots represent independent experiments (**A, D, I-J**), individual cells (**H**), or the mean of independent experiments (**B, F**). P values were calculated using one-sample t-test (**J**), two-tailed unpaired t-test (**H**), or two-tailed

paired t-test (**A, D, I**) except for comparison made with normalizing condition (vehicle) where one-sample t-test was applied. *, P < 0.05. **, P < 0.01. ***, P < 0.001. ****, P < 0.0001. ns, not significant.

FIGURE 2: TBXA2R activates ERMs through RhoA and its kinase effectors SLK/LOK.

(**A**) ebBRET signals measured in parental HEK293 cells or HEK293 cells knock-out for Gq/11 (ΔGq/11) or G12/13 (ΔG12/13), co-expressing TBXA2R and MyrPB-ezrin-rLucII biosensor and treated with 100 nM U46619 for 5 min and/or 1 µM YM-254890 for 30 min. ebBRET signals measured in each cell line are normalized to the vehicle in the same cell line.

(**B-C**) ebBRET signals measured in HEK293T-TBXA2R expressing MyrPB-ezrin-rLucII biosensor and treated with 100 nM U46619 for 5 min and/or 1 µg/mL C3 transferase for 6h (**B**) or 10 µM Y-27632 for 4h (**C**).

(**D**) ebBRET signals measured in HEK293T-TBXA2R expressing MyrPB-ezrin-rLucII biosensor, transiently transfected with non-target siRNA (NT) or siRNA targeting SLK and/or LOK and treated with 100 nM U46619 for 5 min.

(**E-F**) Immunoblot of HEK293T-TBXA2R cells transiently transfected with non-target siRNA (NT) or siRNA targeting SLK and/or LOK and treated with 100 nM U46619 for 5 min (**E**). p-ERM over ERM signals were quantified and normalized to NT incubated with vehicle (**F**).

(**G**) Proposed model for the signaling pathway downstream of TBXA2R and activating ERMs in HEK293T-TBXA2R cells.

ebBRET signals (**A-D**) represent the mean +/- s.d. of at least three independent experiments. Immunoblot (**E**) is representative of three independent experiments. P-ERM quantifications (**F**) represent the mean +/- s.d. of three independent experiments. Dots represent independent experiments (**A-D, F**). P values were calculated using a one-sample t-test (**A**), two-tailed paired t-test (**B-C**) or using Holm-Sidak's multiple comparisons test with a single pooled variance (**D, F**) except for comparison made with

normalizing condition (vehicle, **B**-**C**; NT + vehicle, **D,F**) where a one-sample t-test was applied. *, P < 0.05. **, P < 0.01. ***, P < 0.001. ****, P < 0.0001. ns, not significant.

FIGURE 3: TBXA2R activates ERMs in Hs578T triple-negative breast cancer cells.

(**A-B**) Immunoblot of Hs578T cells treated with vehicle, 100 nM U46619 for 5 min and/or 1 µM SQ-29548 for 30 min (**A**). p-ERM over ERM signals were quantified and normalized to the vehicle (**B**).

(**C-D**) Immunofluorescence of Hs578T cells incubated with vehicle or 100 nM U46619 for 5 min (**C**). p-ERM staining at the cell periphery was quantified and normalized to cells treated with vehicle (**D**).

(**E-F**) Immunoblot of Hs578T cells treated with U46619 for 5 min with the indicated concentrations (**E**). p-ERM over ERM signals were quantified and normalized to the vehicle (**F**).

(**G-L**) Immunoblots of Hs578T cells treated with 100 nM U46619 for 5 min, 1 µM YM-254890 for 30 min, and/or transfected with 1 µg p115-RGS-CAAX (**G**), treated with 100 nM U46619 for 5 min, 1 µg/mL C3 transferase for 6h and/or 10 µM Y-27632 for 4h (**I**), or transiently transfected with non-target siRNA (NT) or two independent siRNA targeting SLK and treated with vehicle or 100 nM U46619 for 5 min (**K**). p-ERM over ERM signals were quantified and normalized to the vehicle (**H, J**) or NT incubated with vehicle (**L**).

(M) Immune complex kinase assay of endogenous SLK immunoprecipitated from Hs578T cells incubated with vehicle or 100 nM U46619 for 5 min. The total lysate (input) is shown in the right panel. p-ERM signals over ponceau staining were quantified and normalized to immunoprecipitated SLK treated with vehicle (lane 2).

Immunoblots (**A, E, G, I, K, M**) and immunofluorescences (**C**) are representative of at least two independent experiments. P-ERM quantifications (**B**, **D**, **F**, **H**, **J**, **L**, **M**) represent the mean +/- s.d. of at least two independent experiments. Dots represent independent experiments (**B, H, J, L-M**), individual cells (**D**), or the mean of independent experiments (**F**). P values were calculated using Holm-Sidak's multiple comparisons test with a single pooled variance (**B, H, J, L**), a two-tailed unpaired t-test (**D**) or a one-sample t-test (**M**)

except for comparison made with normalizing condition (vehicle, **B, H, J**; NT + vehicle, **L**) where one-sample t-test was applied. *, P < 0.05. **, P < 0.01. ***, P < 0.001. ****, P < 0.0001. ns, not significant.

FIGURE 4: Moesin mediates TBXA2R-induced motility and invasion of TNBC cells *in vitro.*

(**A-B**) Immunoblot of Hs578T cells knock-out for ROSA26 (control), EZR, RDX, or MSN and treated with 100 nM U46619 for 5 min (**A**). p-ERM over actin signals were quantified and normalized to ROSA26 + vehicle (**B**).

(**C**) Schematic representation of *in vitro* 2D migration experimental protocol.

(**D-E**) Immunoblot of Hs578T cells knock-out for ROSA26 (control) or MSN using two independent sgRNAs and treated with 100 nM U46619 for 5 min (**D**). p-ERM over actin signals were quantified and normalized to ROSA26 + vehicle (**E**).

(**F**) Illustration of cell migration tracks of Hs578T cells knock-out for ROSA26 (control) or MSN (MSN #1) and treated with 10 nM U46619 for 6 hours. Illustrations are representative of three independent experiments.

(**G-H**) Quantifications of cell velocity during 2D cell migration of Hs578T cells knock-out for ROSA26 (control) or MSN using two independent sgRNAs (**G**) or transiently transfected with non-target siRNA (NT) or two independent siRNA targeting SLK (**H**) and treated with vehicle or 10 nM U46619 for 6 hours.

(**I**) Schematic representation of *in vitro* 3D invasive migration experimental protocol.

(**J-K**) Quantifications of cell velocity during 3D invasive cell migration of Hs578T cells knock-out for ROSA26 (control) or MSN using two independent sgRNAs (**J**) or transiently transfected with non-target siRNA (NT) or two independent siRNA targeting SLK (**K**) and treated with vehicle or 10 nM U46619 for 24 hours.

Immunoblots (**A, D**) are representative of at least two independent experiments. P-ERM quantifications (**B**, **E**) represent the mean +/- s.d. of at least two independent experiments. Velocity quantifications (**G-H**, **J-K**) represent the mean +/- s.d. of three

independent experiments. Dots represent independent experiments (**B, E**) or individual cells (**G-H**, **J-K**). P values were calculated using Holm-Sidak's multiple comparisons test with a single pooled variance (**B**, **E**, **G-H**, **J-K**) except for comparison made with normalizing condition (ROSA26 + vehicle, **B, E**) where a one-sample t-test was applied. *, $P < 0.05$. **, $P < 0.01$. ***, $P < 0.001$. ****, $P < 0.0001$. ns, not significant.

FIGURE 5: TBXA2R-induced metastasis of TNBC cells is mediated by Moesin *in vivo*.

(**A-C**) Analysis of TBXA2R and MSN mRNA expressions in TNBC patients and associated overall survival. Data extracted from The Cancer Genome Atlas (TCGA). (**A**) TNBC breast cancers present higher TBXA2R mRNA expression when compared to normal breast tissue. (**B**) Among TNBC, there is a group of tumors with increased expression of TBXA2R mRNA when compared with normal breast tissue. (**C**) Kaplan–Meier curve shows that TNBC patients with high expression of both TBXA2R and MSN presented shorter overall survival.

(**D-E**) Representative IHC staining of p-ERM and TBXA2R in triple-negative breast cancer tissue (**D**). p-ERM and TBXA2R signal intensities were quantified at the cell cortex (n=55, **E**). Linear regression and Pearson correlation score are represented on the graph.

(**F**) Schematic representation of the *in vivo* metastasis assay. NSG mice were injected with Hs578T cells knock-out for ROSA26 (control) or MSN using two independent sgRNAs. From two days before injection until euthanasia, mice were treated with vehicle or U46619 administered at 50 µg/kg through drinking water. n = 8 mice for ROSA26 + vehicle, n = 10 mice for all other condition.

(**G-I**) Characterization of tumor nodules observed in the livers of mice treated as described in **F**. (**G**) Representative H&E staining of liver sections. Black lines highlight tumor nodules. (**H-I**) The surface of individual tumor nodules was measured using NDP.view 2 (Hamamatsu Photonics) on H&E-stained liver sections and represented as individual tumor nodule (**H**) or represented as a ratio of the total surface of nodules over total surface of liver per animal (expressed in %) (**I**). Quantifications represent the

mean +/- s.e.m of 8 or 10 animals. Total number of liver tumor nodules (n) are indicated in grey (**H**).

(**J-K**) Representative IHC staining for Ki-67 in liver sections from mice described in **C**. Black lines demarcates the tumor (left) from the adjacent normal tissue (right) (**G**). The proliferation index (Ki-67$^+$ cells expressed in %) was then quantified (**H**). Quantifications represent the mean +/- s.e.m of 8 or 10 animals.

Dots represent independent samples (**A, E**), individual tumor nodules (**H**) or individual animals (**I, K**). P values were calculated using two-tailed unpaired t-test (**A**), Log-rank (Mantel-Cox) test (**C**), Pearson correlation (**E**), Welch's t-test because of unequal sample sizes (**H**) or Holm-Sidak's multiple comparisons test with a single pooled variance (**I, K**). *, $P < 0.05$. **, $P < 0.01$. ****, $P < 0.0001$. ns, not significant.

SUPPLEMENTARY FIGURE 1

(**A**) Schematic representation of MyrPB-E,R,M-rLucII ebBRET biosensors (adapted from Leguay, JCS 2021).

(**B-C**) ebBRET signals measured in HEK293T-TBXA2R cells expressing MyrPB-radixin-rLucII (**B**) or MyrPB-moesin-rLucII (**C**) biosensor and treated with 100 nM U46619 for 5 min and/or 100 nM staurosporine for 30 min.

ebBRET signals (**B**-**C**) represent the mean +/- s.d. of three independent experiments. Dots represent independent experiments (**B**-**C**). P values were calculated using a two-tailed paired t-test (**B**-**C**) except for comparison made with normalizing condition (vehicle) where a one-sample t-test was applied. *, $P < 0.05$. ****, $P < 0.0001$. ns, not significant.

SUPPLEMENTARY FIGURE 2

(**A-B**) Immunoblot of MDA-MB-231 cells treated with vehicle, 100 nM U46619 for 5 min and/or 1 µM SQ-29548 for 30 min (**A**). p-ERM over ERM signals were quantified and normalized to the vehicle (**B**).

(**C-D**) Immunofluorescence of MDA-MB-231 cells incubated with vehicle or 100 nM U46619 for 5 min (**C**). p-ERM staining at the cell periphery was quantified and normalized to cells treated with vehicle (**D**).

Immunoblots (**A**) and immunofluorescences (**C**) are representative of three independent experiments. P-ERM quantifications (**B**) represent the mean +/- s.d. of three independent experiments. Dots represent independent experiments (**B**) or individual cells (**D**). P values were calculated using a two-tailed unpaired t-test (**D**) or two-tailed paired t-test (**B**) except for comparison made with normalizing condition (vehicle), where a one-sample t-test was applied. ****, $P < 0.0001$. ns, not significant.

SUPPLEMENTARY FIGURE 3

(**A**) Immunoblot of Hs578T stably expressing non-target shRNA (NT) or shRNA targeting EZR, RDX, or MSN.

(**B**) mRNA expression of EZR, RDX, and MSN in the Hs578T cell line. Data extracted from single-cell RNAseq (Athar, Nucleic Acids Res 2019).

(**C-D**) Immunoblot of Hs578T cells treated with 100 nM U46619 for the indicated time (**C**). p-ERM over ERM signals were quantified and normalized to the vehicle (t=0) (**D**).

(**E-F**) TIDE analysis (Brinkman et al, Nucleic Acids Research 2014) to characterize genomic editing of Hs578T knock-out for MSN using two independent sgRNAs (#1 and #2).

(**G**) Quantifications of cell velocity during 2D cell migration of Hs578T cells stably expressing non-target shRNA (NT) or an shRNA targeting MSN and treated with vehicle or 10 nM U46619 for 6 hours.

Immunoblots (**A**, **C**) are representative of three independent experiments. Velocity quantifications (**G**) represent the mean +/- s.d. of three independent experiments. Dots represent the mean of two independent experiments (**D**) or individual cells (**G**). P values were calculated using Holm-Sidak's multiple comparisons test with a single pooled variance (**G**). ***, P < 0.001. ****, P < 0.0001. ns, not significant.

SUPPLEMENTARY FIGURE 4

(**A**) Measurement of body weights throughout the *in vivo* experiment. Data represent mean +/- s.d. of all animals.

(**B**) Measurement of liver/body weight ratios. At the time of euthanasia, mice were weighed, and the livers were excised and weighed. Data represent mean +/- s.e.m. of all animals.

(**C**) Quantification of tumor nodules observed in livers from mice described in **Fig 5F**.

(**D**) Cell proliferation of Hs578T cells knock-out for ROSA26 (control) or MSN using two independent sgRNAs measured *in vitro* for 6 days. Data represent the mean +/- s.d. of three independent experiments.

Dots represent the mean of independent animals (**A**), individual animals (**B, C**) or the mean of three independent experiments (**D**). P values were calculated using a two-tailed paired t-test (**A, D**) or using Holm-Sidak's multiple comparisons test with a single pooled variance (**B, C**). *, P < 0.05. **, P < 0.01. ns, not significant.

REFERENCES

Algrain, M., O. Turunen, A. Vaheri, D. Louvard, and M. Arpin. 1993. Ezrin contains cytoskeleton and membrane binding domains accounting for its proposed role as a membrane-cytoskeletal linker. *J Cell Biol*. 120:129-139.

Anderson, R.L., T. Balasas, J. Callaghan, R.C. Coombes, J. Evans, J.A. Hall, S. Kinrade, D. Jones, P.S. Jones, R. Jones, J.F. Marshall, M.B. Panico, J.A. Shaw, P.S. Steeg, M. Sullivan, W. Tong, A.D. Westwell, J.W.A. Ritchie, U.K. Cancer Research, and C.R.C.A.M.W.G. Cancer Therapeutics. 2019. A framework for the development of effective anti-metastatic agents. *Nat Rev Clin Oncol*. 16:185-204.

Arpin, M., D. Chirivino, A. Naba, and I. Zwaenepoel. 2011. Emerging role for ERM proteins in cell adhesion and migration. *Cell Adh Migr*. 5:199-206.

Atwood, B.K., J. Lopez, J. Wager-Miller, K. Mackie, and A. Straiker. 2011. Expression of G protein-coupled receptors and related proteins in HEK293, AtT20, BV2, and N18 cell lines as revealed by microarray analysis. *BMC genomics*. 12:14.

Avet, C., A. Mancini, B. Breton, C. Le Gouill, A.S. Hauser, C. Normand, H. Kobayashi, F. Gross, M. Hogue, V. Lukasheva, S. Morissette, E. Fauman, J.-P. Fortin, S. Schann, X. Leroy, D.E. Gloriam, and M. Bouvier. 2020. Selectivity Landscape of 100 Therapeutically Relevant GPCR Profiled by an Effector Translocation-Based BRET Platform.2020.2004.2020.052027.

Avet, C., A. Mancini, B. Breton, C. Le Gouill, A.S. Hauser, C. Normand, H. Kobayashi, F. Gross, M. Hogue, V. Lukasheva, S. St-Onge, M. Carrier, M. Heroux, S. Morissette, E.B. Fauman, J.P. Fortin, S. Schann, X. Leroy, D.E. Gloriam, and M. Bouvier. 2022. Effector membrane translocation biosensors reveal G protein and betaarrestin coupling profiles of 100 therapeutically relevant GPCRs. *Elife*. 11.

Bagci, H., N. Sriskandarajah, A. Robert, J. Boulais, I.E. Elkholi, V. Tran, Z.Y. Lin, M.P. Thibault, N. Dube, D. Faubert, D.R. Hipfner, A.C. Gingras, and J.F. Cote. 2020. Mapping the proximity interaction network of the Rho-family GTPases reveals signalling pathways and regulatory mechanisms. *Nat Cell Biol*. 22:120-134.

Barik, G.K., O. Sahay, D. Paul, and M.K. Santra. 2022. Ezrin gone rogue in cancer progression and metastasis: An enticing therapeutic target. *Biochim Biophys Acta Rev Cancer*. 1877:188753.

Bartholow, T.L., M.J. Becich, U.R. Chandran, and A.V. Parwani. 2011. Immunohistochemical analysis of ezrin-radixin-moesin-binding phosphoprotein 50 in prostatic adenocarcinoma. *Bmc Urol*. 11.

Bartova, M., J. Hlavaty, Y. Tan, C. Singer, K. Pohlodek, J. Luha, and I. Walter. 2017. Expression of ezrin and moesin in primary breast carcinoma and matched lymph node metastases. *Clinical & experimental metastasis*. 34:333-344.

Bianchini, G., C. De Angelis, L. Licata, and L. Gianni. 2022. Treatment landscape of triple-negative breast cancer - expanded options, evolving needs. *Nat Rev Clin Oncol*. 19:91-113.

Breton, B., E. Sauvageau, J. Zhou, H. Bonin, C. Le Gouill, and M. Bouvier. 2010. Multiplexing of multicolor bioluminescence resonance energy transfer. *Biophys J*. 99:4037-4046.

Bruce, B., G. Khanna, L. Ren, G. Landberg, K. Jirstrom, C. Powell, A. Borczuk, E.T. Keller, K.J. Wojno, P. Meltzer, K. Baird, A. McClatchey, A. Bretscher, S.M. Hewitt, and C. Khanna. 2007. Expression of the cytoskeleton linker protein ezrin in human cancers. *Clinical & experimental metastasis*. 24:69-78.

Cancer Genome Atlas, N. 2012. Comprehensive molecular portraits of human breast tumours. *Nature*. 490:61-70.

Cant, S.H., and J.A. Pitcher. 2005. G protein-coupled receptor kinase 2-mediated phosphorylation of ezrin is required for G protein-coupled receptor-dependent reorganization of the actin cytoskeleton. *Mol Biol Cell*. 16:3088-3099.

Carreno, S., I. Kouranti, E.S. Glusman, M.T. Fuller, A. Echard, and F. Payre. 2008. Moesin and its activating kinase Slik are required for cortical stability and microtubule organization in mitotic cells. *J Cell Biol*. 180:739-746.

Clark, A.G., and D.M. Vignjevic. 2015. Modes of cancer cell invasion and the role of the microenvironment. *Curr Opin Cell Biol*. 36:13-22.

Clucas, J., and F. Valderrama. 2014. ERM proteins in cancer progression. *J Cell Sci*. 127:267-275.

Coleman, R.A., P.P. Humphrey, I. Kennedy, G.P. Levy, and P. Lumley. 1981. Comparison of the actions of U-46619, a prostaglandin H2-analogue, with those of prostaglandin H2 and thromboxane A2 on some isolated smooth muscle preparations. *British journal of pharmacology*. 73:773-778.

Curto, M., and A.I. McClatchey. 2004. Ezrin...a metastatic detERMinant? *Cancer Cell*. 5:113-114.

Dai, X., H. Cheng, Z. Bai, and J. Li. 2017. Breast Cancer Cell Line Classification and Its Relevance with Breast Tumor Subtyping. *J Cancer*. 8:3131-3141.

De Jamblinne, C.V., B. Decelle, M. Dehghani, M. Joseph, N. Sriskandarajah, K. Leguay, B. Rambaud, S. Lemieux, P.P. Roux, D.R. Hipfner, and S. Carreno. 2020. STRIPAK regulates Slik localization to control mitotic morphogenesis and epithelial integrity. *J Cell Biol*. 219.

Devost, D., R. Sleno, D. Petrin, A. Zhang, Y. Shinjo, R. Okde, J. Aoki, A. Inoue, and T.E. Hebert. 2017. Conformational Profiling of the AT1 Angiotensin II Receptor Reflects Biased Agonism, G Protein Coupling, and Cellular Context. *J Biol Chem*. 292:5443-5456.

Dovizio, M., S. Alberti, A. Sacco, P. Guillem-Llobat, S. Schiavone, T.J. Maier, D. Steinhilber, and P. Patrignani. 2015. Novel insights into the regulation of cyclooxygenase-2 expression by platelet-cancer cell cross-talk. *Biochem Soc Trans*. 43:707-714.

Ekambaram, P., W. Lambiv, R. Cazzolli, A.W. Ashton, and K.V. Honn. 2011. The thromboxane synthase and receptor signaling pathway in cancer: an emerging paradigm in cancer progression and metastasis. *Cancer metastasis reviews*. 30:397-408.

Elliott, B.E., J.A. Meens, S.K. SenGupta, D. Louvard, and M. Arpin. 2005. The membrane cytoskeletal crosslinker ezrin is required for metastasis of breast carcinoma cells. *Breast cancer research : BCR*. 7:R365-373.

Estecha, A., L. Sanchez-Martin, A. Puig-Kroger, R.A. Bartolome, J. Teixido, R. Samaniego, and P. Sanchez-Mateos. 2009. Moesin orchestrates cortical polarity of melanoma tumour cells to initiate 3D invasion. *J Cell Sci*. 122:3492-3501.

Fehon, R.G., A.I. McClatchey, and A. Bretscher. 2010. Organizing the cell cortex: the role of ERM proteins. *Nat Rev Mol Cell Biol*. 11:276-287.

Fife, C.M., J.A. McCarroll, and M. Kavallaris. 2014. Movers and shakers: cell cytoskeleton in cancer metastasis. *British journal of pharmacology*. 171:5507-5523.

Gales, C., R.V. Rebois, M. Hogue, P. Trieu, A. Breit, T.E. Hebert, and M. Bouvier. 2005. Real-time monitoring of receptor and G-protein interactions in living cells. *Nat Methods*. 2:177-184.

Gary, R., and A. Bretscher. 1995. Ezrin self-association involves binding of an N-terminal domain to a normally masked C-terminal domain that includes the F-actin binding site. *Mol Biol Cell*. 6:1061-1075.

Gay, L.J., and B. Felding-Habermann. 2011. Contribution of platelets to tumour metastasis. *Nat Rev Cancer*. 11:123-134.

Ghaffari, A., V. Hoskin, G. Turashvili, S. Varma, J. Mewburn, G. Mullins, P.A. Greer, F. Kiefer, A.G. Day, Y. Madarnas, S. SenGupta, and B.E. Elliott. 2019. Intravital imaging reveals systemic ezrin inhibition impedes cancer cell migration and lymph node metastasis in breast cancer. *Breast cancer research : BCR*. 21:12.

Guillem-Llobat, P., M. Dovizio, A. Bruno, E. Ricciotti, V. Cufino, A. Sacco, R. Grande, S. Alberti, V. Arena, M. Cirillo, C. Patrono, G.A. FitzGerald, D. Steinhilber, A. Sgambato, and P. Patrignani. 2016. Aspirin prevents colorectal cancer metastasis in mice by splitting the crosstalk between platelets and tumor cells. *Oncotarget*. 7:32462-32477.

Hoskin, V., A. Ghaffari, and B.E. Elliott. 2019. Ezrin, more than a metastatic detERMinant? *Oncotarget*. 10:6755-6757.

Hoskin, V., A. Szeto, A. Ghaffari, P.A. Greer, G.P. Cote, and B.E. Elliott. 2015. Ezrin regulates focal adhesion and invadopodia dynamics by altering calpain activity to promote breast cancer cell invasion. *Mol Biol Cell*. 26:3464-3479.

Hughes, L., C. Malone, S. Chumsri, A.M. Burger, and S. McDonnell. 2008. Characterisation of breast cancer cell lines and establishment of a novel isogenic subclone to study migration, invasion and tumourigenicity. *Clinical & experimental metastasis*. 25:549-557.

Jones, R.L., N.H. Wilson, and R.A. Armstrong. 1985. Characterization of thromboxane receptors in human platelets. *Adv Exp Med Biol*. 192:67-81.

Kattelman, E.J., D.L. Venton, and G.C. Le Breton. 1986. Characterization of U46619 binding in unactivated, intact human platelets and determination of binding site affinities of four TXA2/PGH2 receptor antagonists (13-APA, BM 13.177, ONO 3708 and SQ 29,548). *Thrombosis research*. 41:471-481.

Khanna, C., X. Wan, S. Bose, R. Cassaday, O. Olomu, A. Mendoza, C. Yeung, R. Gorlick, S.M. Hewitt, and L.J. Helman. 2004. The membrane-cytoskeleton linker ezrin is necessary for osteosarcoma metastasis. *Nat Med*. 10:182-186.

Kobayashi, H., L.P. Picard, A.M. Schonegge, and M. Bouvier. 2019. Bioluminescence resonance energy transfer-based imaging of protein-protein interactions in living cells. *Nature protocols*. 14:1084-1107.

Kobayashi, H., J. Sagara, H. Kurita, M. Morifuji, M. Ohishi, K. Kurashina, and S. Taniguchi. 2004. Clinical significance of cellular distribution of moesin in patients with oral squamous cell carcinoma. *Clinical Cancer Research*. 10:572-580.

Kunda, P., A.E. Pelling, T. Liu, and B. Baum. 2008. Moesin controls cortical rigidity, cell rounding, and spindle morphogenesis during mitosis. *Curr Biol*. 18:91-101.

Leguay, K., B. Decelle, I.E. Elkholi, M. Bouvier, J.F. Cote, and S. Carreno. 2022. Interphase microtubule disassembly is a signaling cue that drives cell rounding at mitotic entry. *J Cell Biol*. 221.

Leguay, K., B. Decelle, Y.Y. He, A. Pagniez, M. Hogue, H. Kobayashi, C. Le Gouill, M. Bouvier, and S. Carreno. 2021. Development of conformational BRET biosensors that monitor ezrin, radixin and moesin activation in real time. *J Cell Sci*. 134.

Li, H., M.H. Lee, K. Liu, T. Wang, M. Song, Y. Han, K. Yao, H. Xie, F. Zhu, M. Grossmann, M.P. Cleary, W. Chen, A.M. Bode, and Z. Dong. 2017. Inhibiting breast cancer by targeting the thromboxane A2 pathway. *NPJ Precis Oncol*. 1:8.

Liu, D., L. Ge, F. Wang, H. Takahashi, D. Wang, Z. Guo, S.H. Yoshimura, T. Ward, X. Ding, K. Takeyasu, and X. Yao. 2007. Single-molecule detection of phosphorylation-induced plasticity changes during ezrin activation. *FEBS Lett*. 581:3563-3571.

Lucotti, S., C. Cerutti, M. Soyer, A.M. Gil-Bernabe, A.L. Gomes, P.D. Allen, S. Smart, B. Markelc, K. Watson, P.C. Armstrong, J.A. Mitchell, T.D. Warner, A.J. Ridley, and R.J. Muschel. 2019. Aspirin blocks formation of metastatic intravascular niches by inhibiting platelet-derived COX-1/thromboxane A2. *J Clin Invest*. 129:1845-1862.

Lukasheva, V., D. Devost, C. Le Gouill, Y. Namkung, R.D. Martin, J.M. Longpre, M. Amraei, Y. Shinjo, M. Hogue, M. Lagace, B. Breton, J. Aoki, J.C. Tanny, S.A. Laporte, G. Pineyro, A. Inoue, M. Bouvier, and T.E. Hebert. 2020. Signal profiling of the beta1AR reveals coupling to novel signalling pathways and distinct phenotypic responses mediated by beta1AR and beta2AR. *Sci Rep*. 10:8779.

Lutz, S., A. Shankaranarayanan, C. Coco, M. Ridilla, M.R. Nance, C. Vettel, D. Baltus, C.R. Evelyn, R.R. Neubig, T. Wieland, and J.J. Tesmer. 2007. Structure of Galphaq-p63RhoGEF-RhoA complex reveals a pathway for the activation of RhoA by GPCRs. *Science*. 318:1923-1927.

Matsui, T., M. Amano, T. Yamamoto, K. Chihara, M. Nakafuku, M. Ito, T. Nakano, K. Okawa, A. Iwamatsu, and K. Kaibuchi. 1996. Rho-associated kinase, a novel serine/threonine kinase, as a putative target for small GTP binding protein Rho. *EMBO J*. 15:2208-2216.

Meiri, D., C.B. Marshall, D. Mokady, J. LaRose, M. Mullin, A.C. Gingras, M. Ikura, and R. Rottapel. 2014. Mechanistic insight into GPCR-mediated activation of the

microtubule-associated RhoA exchange factor GEF-H1. *Nature communications*. 5:4857.

Nakahata, N. 2008. Thromboxane A2: physiology/pathophysiology, cellular signal transduction and pharmacology. *Pharmacology & therapeutics*. 118:18-35.

Nakamura, F., M.R. Amieva, and H. Furthmayr. 1995. Phosphorylation of threonine 558 in the carboxyl-terminal actin-binding domain of moesin by thrombin activation of human platelets. *J Biol Chem*. 270:31377-31385.

Namkung, Y., C. Le Gouill, V. Lukashova, H. Kobayashi, M. Hogue, E. Khoury, M. Song, M. Bouvier, and S.A. Laporte. 2016. Monitoring G protein-coupled receptor and beta-arrestin trafficking in live cells using enhanced bystander BRET. *Nature communications*. 7:12178.

Namkung, Y., C. LeGouill, S. Kumar, Y. Cao, L.B. Teixeira, V. Lukasheva, J. Giubilaro, S.C. Simoes, J.M. Longpre, D. Devost, T.E. Hebert, G. Pineyro, R. Leduc, C.M. Costa-Neto, M. Bouvier, and S.A. Laporte. 2018. Functional selectivity profiling of the angiotensin II type 1 receptor using pathway-wide BRET signaling sensors. *Science signaling*. 11.

Nie, D., M. Che, A. Zacharek, Y. Qiao, L. Li, X. Li, M. Lamberti, K. Tang, Y. Cai, Y. Guo, D. Grignon, and K.V. Honn. 2004. Differential expression of thromboxane synthase in prostate carcinoma: role in tumor cell motility. *Am J Pathol*. 164:429-439.

Ogletree, M.L., D.N. Harris, R. Greenberg, M.F. Haslanger, and M. Nakane. 1985. Pharmacological actions of SQ 29,548, a novel selective thromboxane antagonist. *The Journal of pharmacology and experimental therapeutics*. 234:435-441.

Orr, K., N.E. Buckley, P. Haddock, C. James, J.L. Parent, S. McQuaid, and P.B. Mullan. 2016. Thromboxane A2 receptor (TBXA2R) is a potent survival factor for triple negative breast cancers (TNBCs). *Oncotarget*. 7:55458-55472.

Pang, S.T., X. Fang, A. Valdman, G. Norstedt, A. Pousette, L. Egevad, and P. Ekman. 2004. Expression of ezrin in prostatic intraepithelial neoplasia. *Urology*. 63:609-612.

Papatheodorou, I., P. Moreno, J. Manning, A.M. Fuentes, N. George, S. Fexova, N.A. Fonseca, A. Fullgrabe, M. Green, N. Huang, L. Huerta, H. Iqbal, M. Jianu, S. Mohammed, L. Zhao, A.F. Jarnuczak, S. Jupp, J. Marioni, K. Meyer, R. Petryszak, C.A. Prada Medina, C. Talavera-Lopez, S. Teichmann, J.A. Vizcaino, and A. Brazma. 2020. Expression Atlas update: from tissues to single cells. *Nucleic Acids Res*. 48:D77-D83.

Park, J., J.H. Jang, S. Oh, M. Kim, C. Shin, M. Jeong, K. Heo, J.B. Park, S.R. Kim, and Y.S. Oh. 2018. LPA-induced migration of ovarian cancer cells requires activation of ERM proteins via LPA1 and LPA2. *Cellular signalling*. 44:138-147.

Pulix, M., V. Lukashchuk, D.C. Smith, and A.J. Dickson. 2021. Molecular characterization of HEK293 cells as emerging versatile cell factories. *Current opinion in biotechnology*. 71:18-24.

Qin, Y., W. Chen, G. Jiang, L. Zhou, X. Yang, H. Li, X. He, H.L. Wang, Y.B. Zhou, S. Huang, and S. Liu. 2020. Interfering MSN-NONO complex-activated CREB signaling serves as a therapeutic strategy for triple-negative breast cancer. *Sci Adv*. 6:eaaw9960.

Ren, L., and C. Khanna. 2014. Role of ezrin in osteosarcoma metastasis. *Adv Exp Med Biol*. 804:181-201.

Retzer, M., and M. Essler. 2000. Lysophosphatidic acid-induced platelet shape change proceeds via Rho/Rho kinase-mediated myosin light-chain and moesin phosphorylation. *Cellular signalling*. 12:645-648.

Roubinet, C., B. Decelle, G. Chicanne, J.F. Dorn, B. Payrastre, F. Payre, and S. Carreno. 2011. Molecular networks linked by Moesin drive remodeling of the cell cortex during mitosis. *J Cell Biol*. 195:99-112.

Sah, V.P., T.M. Seasholtz, S.A. Sagi, and J.H. Brown. 2000. The role of Rho in G protein-coupled receptor signal transduction. *Annual review of pharmacology and toxicology*. 40:459-489.

Schrage, R., A.L. Schmitz, E. Gaffal, S. Annala, S. Kehraus, D. Wenzel, K.M. Bullesbach, T. Bald, A. Inoue, Y. Shinjo, S. Galandrin, N. Shridhar, M. Hesse, M. Grundmann, N. Merten, T.H. Charpentier, M. Martz, A.J. Butcher, T. Slodczyk, S. Armando, M. Effern, Y. Namkung, L. Jenkins, V. Horn, A. Stossel, H. Dargatz, D. Tietze, D. Imhof, C. Gales, C. Drewke, C.E. Muller, M. Holzel, G. Milligan, A.B. Tobin, J. Gomeza, H.G. Dohlman, J. Sondek, T.K. Harden, M. Bouvier, S.A. Laporte, J. Aoki, B.K. Fleischmann, K. Mohr, G.M. Konig, T. Tuting, and E. Kostenis. 2015. The experimental power of FR900359 to study Gq-regulated biological processes. *Nature communications*. 6:10156.

Seyfried, T.N., and L.C. Huysentruyt. 2013. On the origin of cancer metastasis. *Critical reviews in oncogenesis*. 18:43-73.

Shaw, R.J., M. Henry, F. Solomon, and T. Jacks. 1998. RhoA-dependent phosphorylation and relocalization of ERM proteins into apical membrane/actin protrusions in fibroblasts. *Mol Biol Cell*. 9:403-419.

Shcherbina, A., D.M. Kenney, A. Bretscher, and O.D.E. Remold. 1999. Dynamic association of moesin with the membrane skeleton of thrombin- activated platelets. *Blood*. 93:2128-2129.

Simons, P.C., S.F. Pietromonaco, D. Reczek, A. Bretscher, and L. Elias. 1998. C-terminal threonine phosphorylation activates ERM proteins to link the cell's cortical lipid bilayer to the cytoskeleton. *Biochem Biophys Res Commun*. 253:561-565.

Solinet, S., K. Mahmud, S.F. Stewman, K. Ben El Kadhi, B. Decelle, L. Talje, A. Ma, B.H. Kwok, and S. Carreno. 2013. The actin-binding ERM protein Moesin binds to and stabilizes microtubules at the cell cortex. *J Cell Biol*. 202:251-260.

Song, Y., X. Ma, M. Zhang, M. Wang, G. Wang, Y. Ye, and W. Xia. 2020. Ezrin Mediates Invasion and Metastasis in Tumorigenesis: A Review. *Front Cell Dev Biol*. 8:588801.

Takasaki, J., T. Saito, M. Taniguchi, T. Kawasaki, Y. Moritani, K. Hayashi, and M. Kobori. 2004. A novel Galphaq/11-selective inhibitor. *J Biol Chem*. 279:47438-47445.

Vaiskunaite, R., V. Adarichev, H. Furthmayr, T. Kozasa, A. Gudkov, and T.A. Voyno-Yasenetskaya. 2000. Conformational activation of radixin by G13 protein alpha subunit. *J Biol Chem*. 275:26206-26212.

van Unen, J., T. Yin, Y.I. Wu, M. Mastop, T.W. Gadella, Jr., and J. Goedhart. 2016. Kinetics of recruitment and allosteric activation of ARHGEF25 isoforms by the heterotrimeric G-protein Galphaq. *Sci Rep*. 6:36825.

Viswanatha, R., P.Y. Ohouo, M.B. Smolka, and A. Bretscher. 2012. Local phosphocycling mediated by LOK/SLK restricts ezrin function to the apical aspect of epithelial cells. *J Cell Biol*. 199:969-984.

Watkins, G., A. Douglas-Jones, R.E. Mansel, and W.G. Jiang. 2005. Expression of thromboxane synthase, TBXAS1 and the thromboxane A2 receptor, TBXA2R, in human breast cancer. *Int Semin Surg Oncol*. 2:23.

Welch, D.R., and D.R. Hurst. 2019. Defining the Hallmarks of Metastasis. *Cancer Res*. 79:3011-3027.

Werfel, T.A., D.J. Hicks, B. Rahman, W.E. Bendeman, M.T. Duvernay, J.G. Maeng, H. Hamm, R.R. Lavieri, M.M. Joly, J.M. Pulley, D.L. Elion, D.M. Brantley-Sieders, and R.S. Cook. 2020. Repurposing of a Thromboxane Receptor Inhibitor Based on a Novel Role in Metastasis Identified by Phenome-Wide Association Study. *Molecular cancer therapeutics*. 19:2454-2464.

Wikstrom, K., D.J. Kavanagh, H.M. Reid, and B.T. Kinsella. 2008. Differential regulation of RhoA-mediated signaling by the TPalpha and TPbeta isoforms of the human thromboxane A2 receptor: independent modulation of TPalpha signaling by prostacyclin and nitric oxide. *Cellular signalling*. 20:1497-1512.

Wilde, C., and K. Aktories. 2001. The Rho-ADP-ribosylating C3 exoenzyme from Clostridium botulinum and related C3-like transferases. *Toxicon*. 39:1647-1660.

Yousef, E.M., M.R. Tahir, Y. St-Pierre, and L.A. Gaboury. 2014. MMP-9 expression varies according to molecular subtypes of breast cancer. *BMC cancer*. 14:609.

Yu, O.M., and J.H. Brown. 2015. G Protein-Coupled Receptor and RhoA-Stimulated Transcriptional Responses: Links to Inflammation, Differentiation, and Cell Proliferation. *Molecular pharmacology*. 88:171-180.

Yu, Y., J. Khan, C. Khanna, L. Helman, P.S. Meltzer, and G. Merlino. 2004. Expression profiling identifies the cytoskeletal organizer ezrin and the developmental homeoprotein Six-1 as key metastatic regulators. *Nat Med*. 10:175-181.

Figure 1

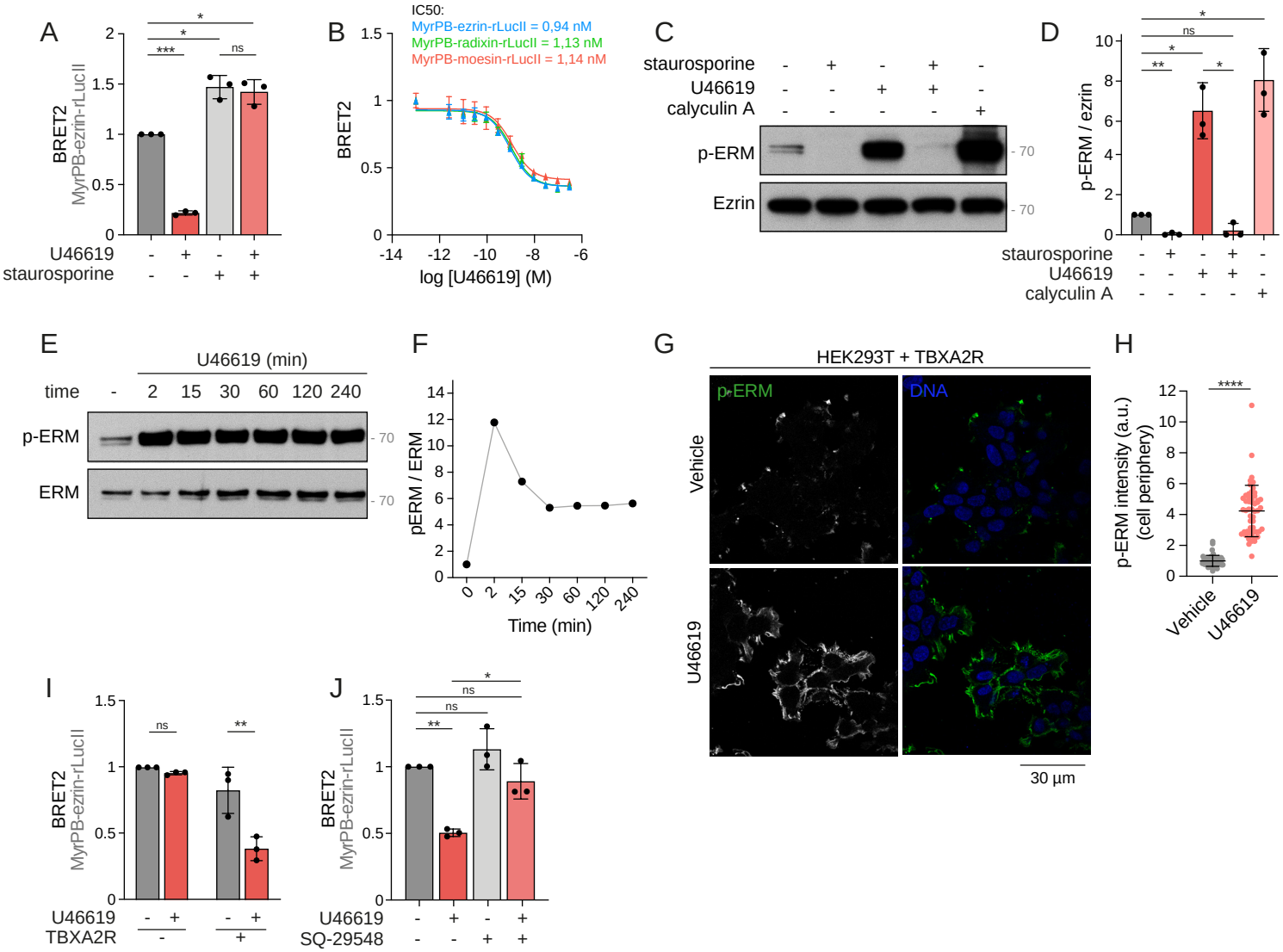
A
BRET2
MyrPB-ezrin-rLucII
U46619
staurosporine
B
IC50:
MyrPB-ezrin-rLucII = 0,94 nM
MyrPB-radixin-rLucII = 1,13 nM
MyrPB-moesin-rLucII = 1,14 nM
BRET2
log [U46619] (M)
C
staurosporine
U46619
calyculin A
p-ERM
Ezrin
D
p-ERM / ezrin
staurosporine
U46619
calyculin A
E
U46619 (min)
time
p-ERM
ERM
F
pERM / ERM
Time (min)
G
HEK293T + TBXA2R
p-ERM
DNA
Vehicle
U46619
30 µm
H
p-ERM intensity (a.u.)
(cell periphery)
Vehicle
U46619
I
BRET2
MyrPB-ezrin-rLucII
U46619
TBXA2R
J
BRET2
MyrPB-ezrin-rLucII
U46619
SQ-29548

Figure 2

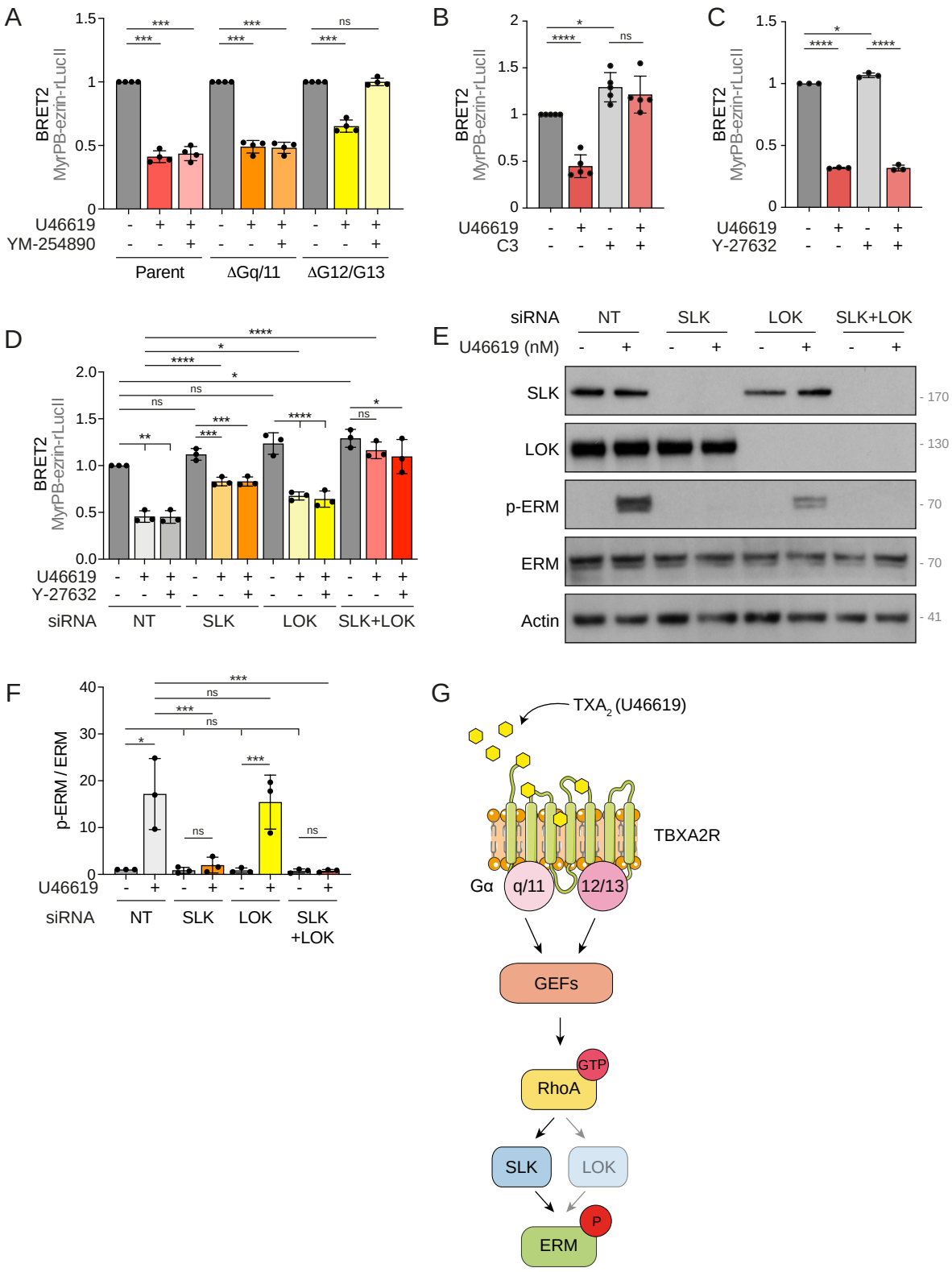
A
BRET2
MyrPB-ezrin-rLucII
U46619
YM-254890
Parent
ΔGq/11
ΔG12/G13
B
C3
C
Y-27632
D
siRNA
NT
SLK
LOK
SLK+LOK
E
U46619 (nM)
p-ERM
ERM
Actin
F
p-ERM / ERM
G
TXA2 (U46619)
TBXA2R
Gα
q/11
12/13
GEFs
GTP
RhoA
P

Figure 3

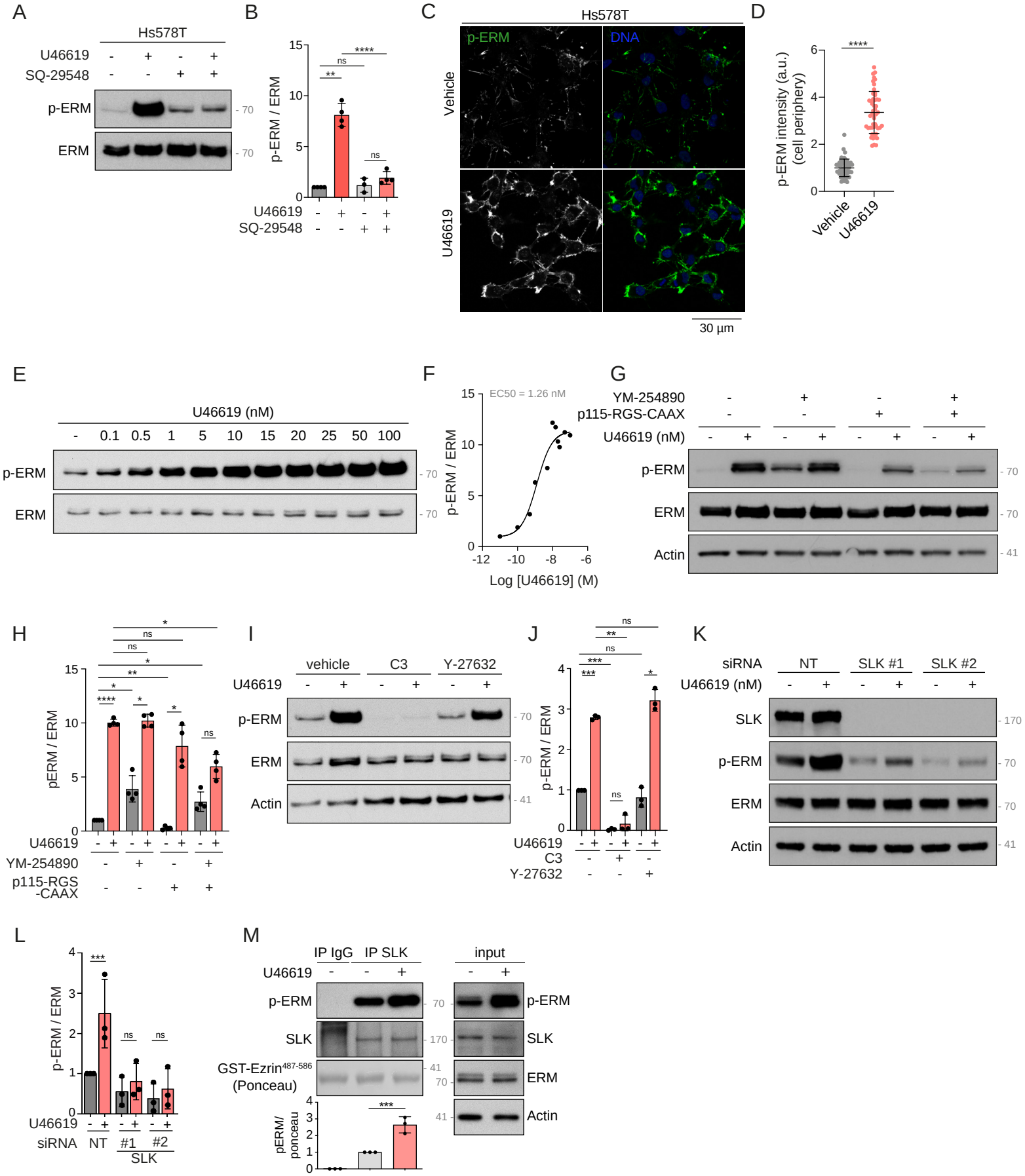
A
Hs578T
U46619 - + - +
SQ-29548 - - + +
p-ERM
ERM
- 70
- 70
B
p-ERM / ERM
15
10
5
0
ns
****
**
ns
U46619 - + - +
SQ-29548 - - + +
C
Hs578T
p-ERM
DNA
Vehicle
U46619
30 µm
D
p-ERM intensity (a.u.)
(cell periphery)
6
4
2
0
****
Vehicle
U46619
E
U46619 (nM)
- 0.1 0.5 1 5 10 15 20 25 50 100
p-ERM
ERM
- 70
- 70
F
EC50 = 1.26 nM
p-ERM / ERM
15
10
5
0
-12 -10 -8 -6
Log [U46619] (M)
G
YM-254890 - + - +
p115-RGS-CAAX - - + +
U46619 (nM) - + - + - + - +
p-ERM
ERM
Actin
- 70
- 70
- 41
H
pERM / ERM
15
10
5
0
*
ns
ns
*
**
*
****
*
*
ns
U46619 - + - + - + - +
YM-254890 - + - +
p115-RGS -CAAX - - + +
I
vehicle C3 Y-27632
U46619 - + - + - +
p-ERM
ERM
Actin
- 70
- 70
- 41
J
p-ERM / ERM
4
3
2
1
0
ns
**
ns
***
***
*
ns
U46619 - + - + - +
C3 - + -
Y-27632 - - +
K
siRNA NT SLK #1 SLK #2
U46619 (nM) - + - + - +
SLK
p-ERM
ERM
Actin
- 170
- 70
- 70
- 41
L
p-ERM / ERM
4
3
2
1
0
***
ns
ns
U46619 - + - + - +
siRNA NT #1 #2
SLK
M
IP IgG IP SLK input
U46619 - - + - +
p-ERM
SLK
GST-Ezrin487-586
(Ponceau)
70
170
41
70
41
p-ERM
SLK
ERM
Actin
pERM/ ponceau
4
3
2
1
0
***

Figure 4

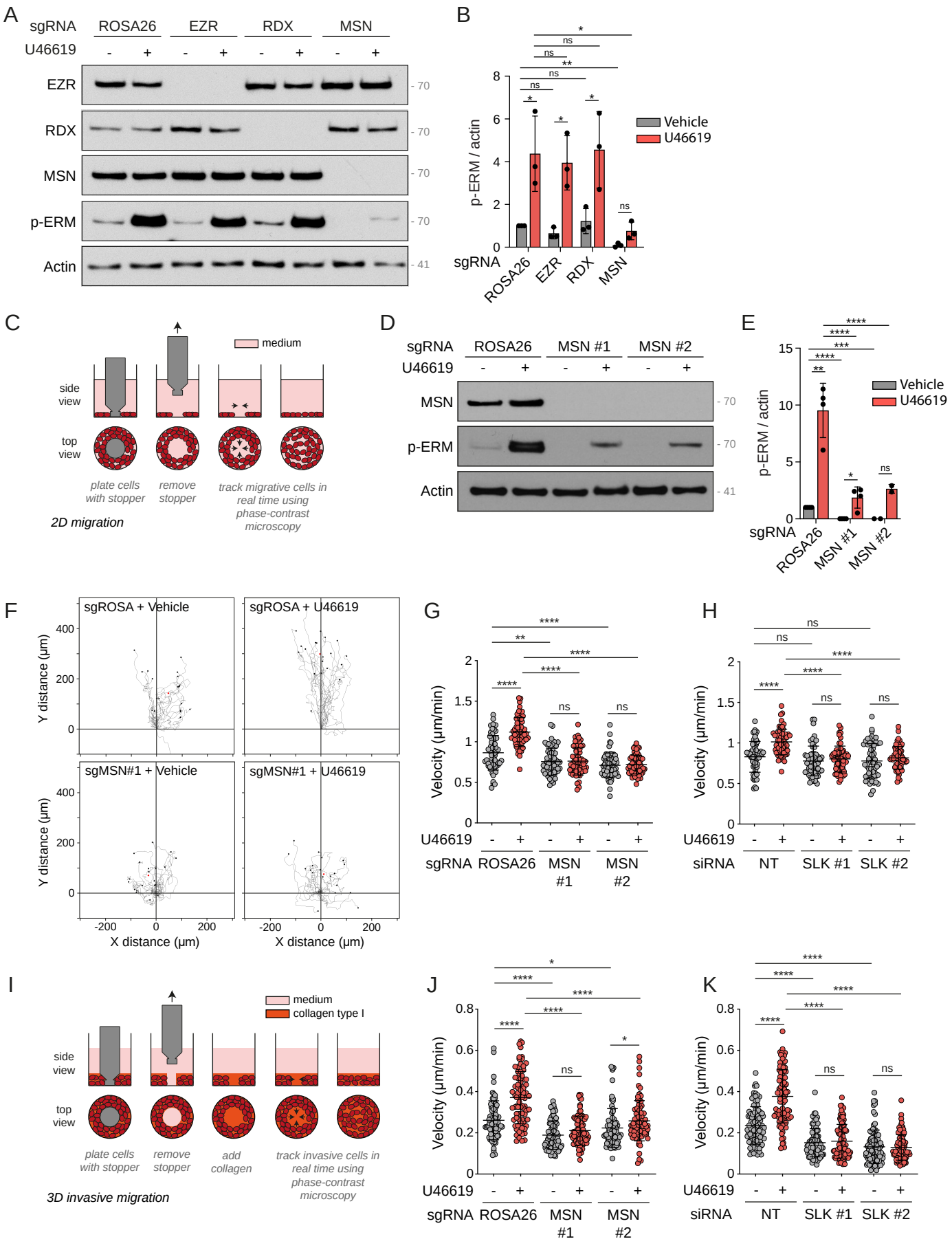
A
sgRNA
ROSA26
EZR
RDX
MSN
U46619
EZR
RDX
MSN
p-ERM
Actin
70
41
B
p-ERM / actin
Vehicle
U46619
sgRNA
ROSA26
EZR
RDX
MSN
C
medium
side view
top view
plate cells with stopper
remove stopper
track migrative cells in real time using phase-contrast microscopy
2D migration
D
sgRNA
ROSA26
MSN #1
MSN #2
U46619
MSN
p-ERM
Actin
E
p-ERM / actin
Vehicle
U46619
sgRNA
ROSA26
MSN #1
MSN #2
F
sgROSA + Vehicle
sgROSA + U46619
sgMSN#1 + Vehicle
sgMSN#1 + U46619
Y distance (µm)
X distance (µm)
G
Velocity (µm/min)
U46619
sgRNA
ROSA26
MSN #1
MSN #2
H
Velocity (µm/min)
U46619
siRNA
NT
SLK #1
SLK #2
I
medium
collagen type I
side view
top view
plate cells with stopper
remove stopper
add collagen
track invasive cells in real time using phase-contrast microscopy
3D invasive migration
J
Velocity (µm/min)
U46619
sgRNA
ROSA26
MSN #1
MSN #2
K
Velocity (µm/min)
U46619
siRNA
NT
SLK #1
SLK #2

Figure 5

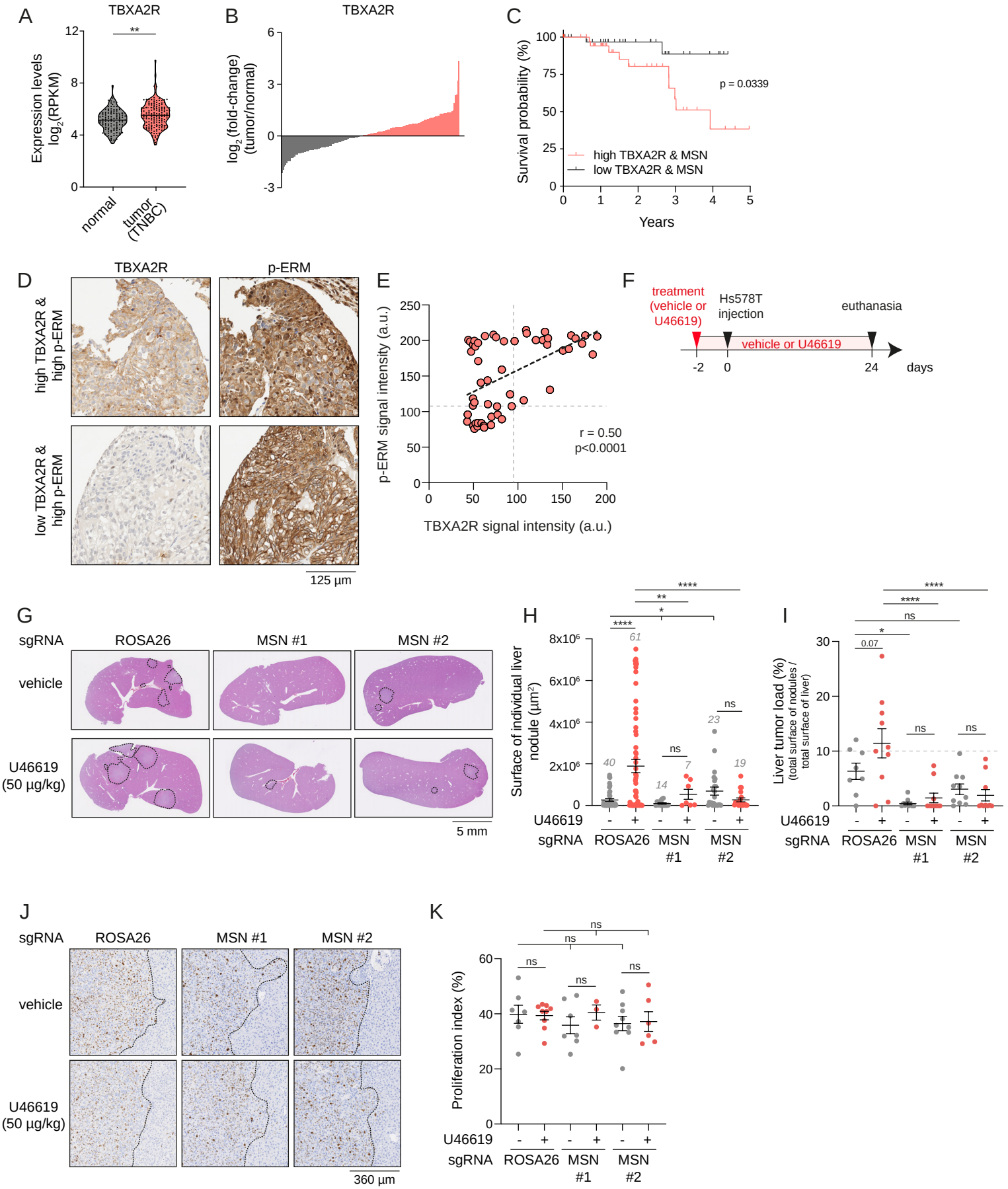
A
TBXA2R
Expression levels log2(RPKM)
normal
tumor (TNBC)
B
TBXA2R
log2 (fold-change) (tumor/normal)
C
Survival probability (%)
p = 0.0339
high TBXA2R & MSN
low TBXA2R & MSN
Years
D
TBXA2R
p-ERM
high TBXA2R & high p-ERM
low TBXA2R & high p-ERM
125 µm
E
p-ERM signal intensity (a.u.)
r = 0.50
p<0.0001
TBXA2R signal intensity (a.u.)
F
treatment (vehicle or U46619)
Hs578T injection
euthanasia
vehicle or U46619
days
G
sgRNA
ROSA26
MSN #1
MSN #2
vehicle
U46619 (50 µg/kg)
5 mm
H
Surface of individual liver nodule (µm²)
U46619
sgRNA
ROSA26
MSN #1
MSN #2
I
Liver tumor load (%) (total surface of nodules / total surface of liver)
J
360 µm
K
Proliferation index (%)